

NATIONAL AERONAUTICS AND SPACE ADMINISTRATION

1N 08
380 304

TECHNICAL REPORT
R-65

DETERMINATION OF LATERAL STABILITY CHARACTERISTICS FROM FREE-FLIGHT MODEL TESTS, WITH EXPERIMENTAL RESULTS ON THE EFFECTS OF WING VERTICAL POSITION AND DIHEDRAL AT TRANSONIC SPEEDS

By CLARENCE L. GILLIS, JESSE L. MITCHELL,
and CHARLES T. D'AIUTOLO

1960

TECHNICAL REPORT R-65

DETERMINATION OF LATERAL STABILITY CHARACTERISTICS FROM FREE-FLIGHT MODEL TESTS, WITH EXPERIMENTAL RESULTS ON THE EFFECTS OF WING VERTICAL POSITION AND DIHEDRAL AT TRANSONIC SPEEDS

**By CLARENCE L. GILLIS, JESSE L. MITCHELL,
and CHARLES T. D'AIUTOLO**

**Langley Research Center
Langley Field, Va.**

TECHNICAL REPORT R-65

DETERMINATION OF LATERAL STABILITY CHARACTERISTICS FROM FREE-FLIGHT MODEL TESTS, WITH EXPERIMENTAL RESULTS ON THE EFFECTS OF WING VERTICAL POSITION AND DIHEDRAL AT TRANSONIC SPEEDS ¹

By CLARENCE L. GILLIS, JESSE L. MITCHELL,
and CHARLES T. D'AUTOLO

SUMMARY

A method of testing and data analysis is presented for investigating the lateral stability characteristics of airplane models in free flight. The time-vector method of solution of the oscillatory lateral motion proved to be a useful method of determining aerodynamic derivatives. The method is illustrated by experimental results at transonic speeds for three swept-wing airplane models differing only in vertical position and dihedral of the wing, and the major effects of these geometric variations were determined. Also shown are experimental results from one unswept-wing airplane model to illustrate the usefulness of direct measurements of forces and moments in establishing the linearity of the results. An interpretation of the experimental results in terms of flying qualities for a full-scale airplane is included.

INTRODUCTION

Attainment of airplane flight speeds in the supersonic realm has focused attention on the stability problems associated with flight at high speeds and high altitudes. The types of lateral motions encountered and the importance of certain of the stability derivatives and inertia relations in defining the motions of the airplane have been examined. (See refs. 1 to 5, for example.) Wind-tunnel techniques are available for measuring the static lateral stability derivatives as well as the rotary lateral stability derivatives (ref. 6). Development of analysis methods and test techniques has been under way for the

purpose of determining airplane lateral stability characteristics, including both static and rotary derivatives, from free-flight tests. Reference 7 gives the fundamentals of a method, the time-vector method, that has proved useful in lateral stability analyses.

The purpose of the present report is to describe the time-vector method of analysis as applied to the oscillatory lateral motions of free-flight airplane models and to present illustrative experimental data as an aid in evaluating the test technique. Three rocket-propelled models of a 45° swept-wing airplane configuration were flown and covered a Mach number range from 0.7 to 1.3. The three models differed in wing position and dihedral. One model had a high wing with no dihedral, one had a low wing with no dihedral, and one had a high wing with 10° negative dihedral. The geometric variations utilized in the program provided appreciable variations in frequency and very large variations in roll-to-yaw amplitude ratios. Some evaluation of the effects of these factors on the usefulness and accuracy of the test technique was possible.

In addition, data are presented for an unswept-wing configuration at transonic speeds to illustrate the value of direct measurements of forces and moments in establishing the linearity of the results.

The models were flight tested at the NASA Wallops Station.

¹ Supersedes declassified NACA Research Memorandum L56E17 by Clarence L. Gillis and Rowe Chapman, Jr., 1956.

SYMBOLS			
a_l	longitudinal accelerometer reading, positive in the positive x -direction, g units	l	longitudinal distance between two transverse accelerometers, ft
a_n	normal accelerometer reading, positive in the negative z -direction, g units	M	Mach number
a_t	transverse accelerometer reading, positive in the positive y -direction, g units	M_X, M_Y, M_Z	rolling, pitching, and yawing moments about X -, Y -, and Z -axes, respectively
a_1	damping factor of oscillatory motion, sec^{-1}	m	mass, slugs
a_2	damping factor of aperiodic motion, sec^{-1}	m_X	rolling moment on a section of the wing, ft-lb (see appendix)
b	wing span, ft	P	period of lateral oscillation, sec
C_c	chord-force coefficient, $-a_l \frac{W}{q'S}$	p	rolling velocity, radians/sec
C_L	lift coefficient, $C_X \cos \alpha - C_c \sin \alpha$	q	pitching velocity, radians/sec
C_l	rolling-moment coefficient, $\frac{\text{Rolling moment}}{q'Sb}$	q'	dynamic pressure, lb/sq ft
C_N	normal-force coefficient, $a_n \frac{W}{q'S}$	R	Reynolds number based on wing mean aerodynamic chord
C_n	yawing-moment coefficient, $\frac{\text{Yawing moment}}{q'Sb}$	r	yawing velocity, radians/sec
C_Y	lateral-force coefficient, $a_t \frac{W}{q'S}$	S	wing area, sq ft
$C_{1/2}$	number of cycles required for oscillation to damp to half amplitude	t	time, sec
c	local chord, ft	$t_{1/2}$	time required for lateral oscillation to damp to half amplitude, sec
\bar{c}	mean aerodynamic chord, ft	V	velocity, ft/sec
g	gravitational acceleration, 32.2 ft/sec ²	v_e	equivalent lateral velocity, ft/sec
h	altitude, ft	W	weight of model, lb
I_X	moment of inertia about X -axis, slug-ft ²	X, Y, Z	coordinate axes
I_Y	moment of inertia about Y -axis, slug-ft ²	y	spanwise station, ft
I_Z	moment of inertia about Z -axis, slug-ft ²	y'	spanwise station at which concentrated load is applied, ft
I_{XZ}	product of inertia, $\frac{1}{2}(I_Z - I_X) \tan 2\epsilon$, slug-ft ²	α	angle of attack, radians or deg
K_1	span-load distribution factor, sq ft (see appendix)	β	angle of sideslip, radians or deg
k_X	radius of gyration about X -axis, ft	β_0	initial value of angle of sideslip, radians or deg
k_Z	radius of gyration about Z -axis, ft	Γ	dihedral angle, deg, or span-load parameter (see appendix)
L	concentrated load, lb (see appendix)	ϵ	principal-axis inclination, positive as shown in figure 1
		$\eta = \frac{y}{c/2}$	
		θ	pitch angle or angle of twist (see appendix), radians
		μ_b	relative mass density, $m/\rho Sb$
		ρ	atmospheric density, slugs/cu ft
		ϕ	roll angle, radians
		ψ	yaw angle, radians
		Ω_{c_Y}	phase angle by which C_Y leads β
		Ω_p	phase angle by which p leads β
		Ω_r	phase angle by which r leads β
		ω	oscillation frequency, radians/sec
		ω_n	undamped natural frequency, radians/sec
		Subscripts:	
		A	full-scale airplane

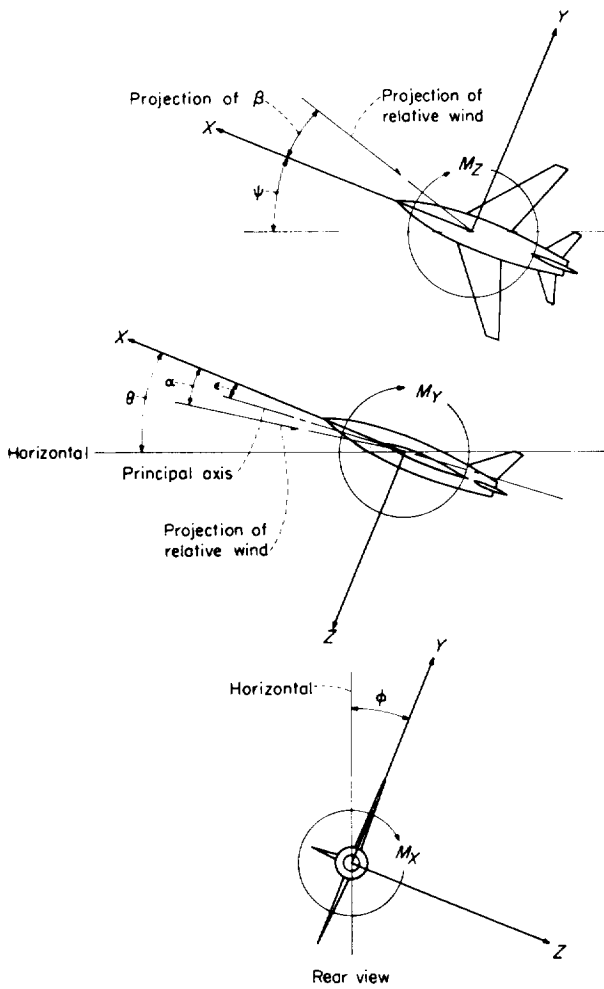


FIGURE 1. —System of body axes.

e	elastic
h	horizontal tail
r	rigid
t	trim value
v	vertical tail
w	wing
wf	wing-fuselage

A single dot over a symbol indicates the derivative of the quantity with respect to time; a double dot represents the second derivative with respect to time.

Amplitude ratios of the oscillatory components of the motion are designated as $\left| \frac{\dot{C}_Y}{\beta} \right|$, $\left| \frac{\dot{p}}{\beta} \right|$, and so forth.

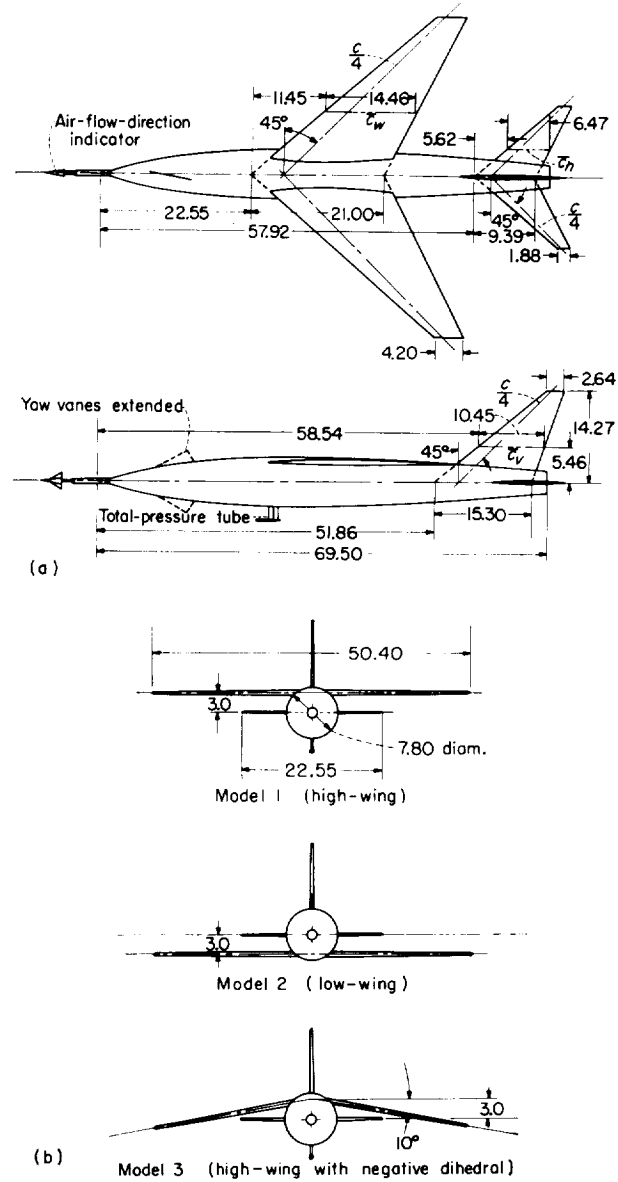
The static stability derivatives are indicated in the following manner: $C_{Y\beta} = \frac{\partial C_Y}{\partial \beta}$, $C_{N\beta} = \frac{\partial C_N}{\partial \beta}$, and

so forth; whereas, the rotary and acceleration derivatives are indicated as: $C_{nr} = \frac{\partial C_n}{\partial r}$, $C_{n\dot{\beta}} = \frac{\partial C_n}{\partial \dot{\beta}}$, and so forth.

MODELS AND TESTS

MODELS

Sketches showing the dimensions of the swept-wing models are presented in figure 2. Additional



(a) Plan and side view of model 1 (high-wing model).
(b) Front views of models.

FIGURE 2. —Swept-wing models. All dimensions are in inches.

geometric characteristics of the models are given in table I and the mass and inertia characteristics are given in table II.

The three swept-wing models had geometrically identical surfaces and fuselages and differed only in the vertical position and dihedral of the wing. The wing weight was counterbalanced so that the model center of gravity was on the geometric center line for all models. The wings were of composite wood and metal construction. Vertical- and horizontal-tail surfaces were machined from solid duralumin. The horizontal-tail surface was set at an incidence angle of $-1/2^\circ$ with the fuselage center line for all models. The fuselage was a parabolic body of revolution with maximum

diameter at 40 percent of the length. Housed in the spun-metal nose of the model was an electrically actuated yaw vane disturber. Photographs of the models are shown in figure 3.

In order to minimize the amount of pitch-yaw coupling encountered in the tests, the center of gravity of each model was placed very far forward (see table II) in an attempt to keep the pitch frequency always higher than twice the yaw frequency and thus avoid a resonant condition (ref. 8). For identification in this report, the high-wing model is designated model 1; the low-wing model, model 2; and the high-wing model with negative dihedral, model 3.

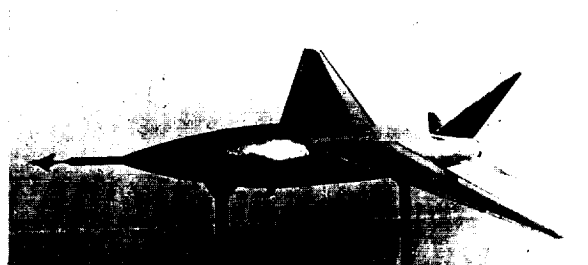
The unswept-wing model, designated model 4,

TABLE I. GEOMETRIC CHARACTERISTICS

	Swept-wing models	Unswept-wing model
Wing:		
Area (extended to model center line), sq ft	4.41	4.25
Aspect ratio	4.0	3.1
Airfoil section	NACA 65A004	4.5-percent-thick hexagonal
Horizontal tail:		
Area (extended to model center line), sq ft	0.88	1.10
Aspect ratio	4.0	4.33
Airfoil section	NACA 65A004	5.0-percent-thick hexagonal
Vertical tail:		
Area (see figs. 2 and 4), sq ft	0.89	0.60
Aspect ratio	1.59	1.30
Airfoil section	NACA 65A004	4.5-percent-thick hexagonal

TABLE II. MASS AND INERTIA CHARACTERISTICS

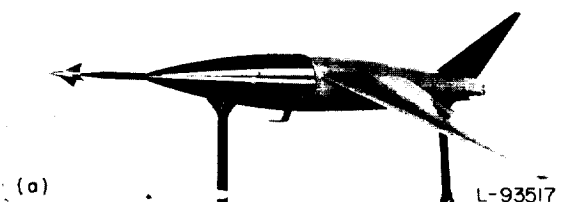
	Swept-wing models			Unswept-wing model
	Model 1	Model 2	Model 3	Model 4
Weight, lb	103.0	111.0	112.7	154.0
Center-of-gravity position, percent \bar{c}	0	3.8	-0.6	1.0
Moments of inertia:				
Pitch, slug-ft ²	5.47	5.88	5.90	
Yaw, slug-ft ²	5.81	6.14	6.38	18.20
Roll, slug-ft ²	0.61	0.66	0.69	1.18
Inclination of principal axis, deg	2.15	0.75	1.60	4.80
Product of inertia	0.20	0.07	0.16	1.44



Model 1



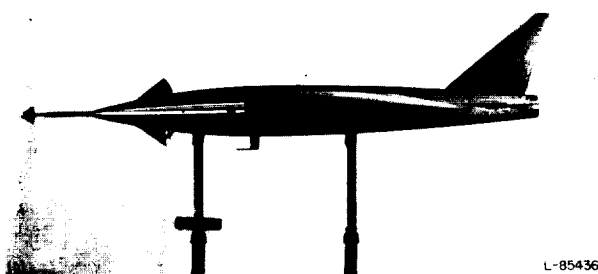
Model 2



Model 3

(a) Three-quarter front views.

FIGURE 3. Photographs of the swept-wing models.



(b) Model 3 with yaw vanes extended.

FIGURE 3. Concluded.

was representative of a supersonic research airplane configuration (ref. 9). A sketch of the 0.16-scale model is shown in figure 4 and a photograph of the model ready for launching is shown in figure 5. The model was of metal construction with the exception of some fiber

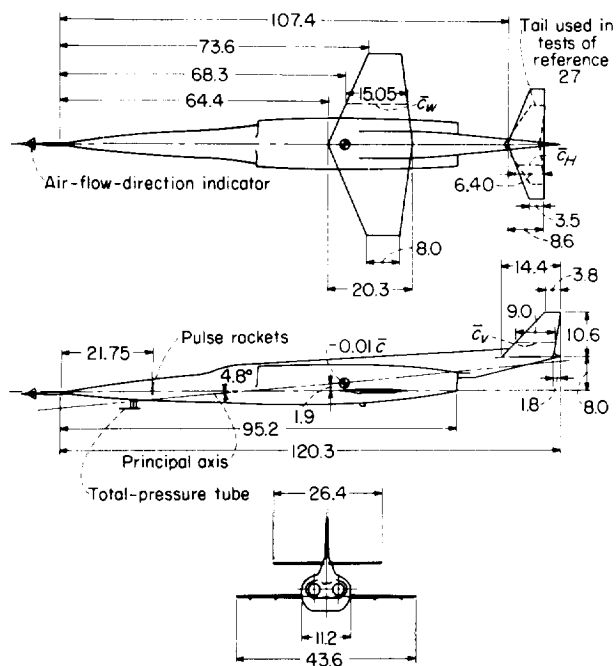


FIGURE 4. Unswept-wing model (model 4). All dimensions are in inches.

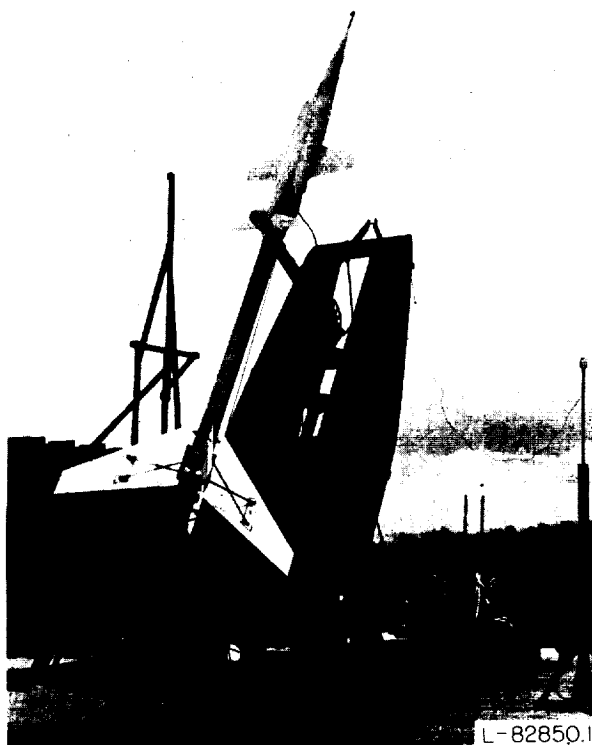


FIGURE 5. Model and booster ready for launching.

glass fairing on the tail boom. The body was made of magnesium castings and duralumin sheet, and the wing and tail surfaces were solid duralumin. Additional geometric characteristics are given in table I and the mass and inertia characteristics are contained in table II. The setting of the horizontal tail was -1.0° . All surfaces had a modified hexagonal airfoil section. The inlets were connected to constant-diameter ducts designed for choked flow at the exits with a mass-flow ratio of about 0.8. In order to provide for disturbances in flight, this model was equipped with 6 pulse rockets located in the nose of the model, each rocket having a total impulse of 6 pound-seconds and a burning time of 0.08 second.

INSTRUMENTATION

Each model contained an eight-channel NASA telemeter. The quantities recorded continuously were total pressure; angle of sideslip; rolling velocity; normal, longitudinal, and transverse accelerations near the center of gravity; transverse acceleration at the nose; yaw-vane-disturber deflection (model 1 only); and angle of attack (models 2, 3, and 4 only).

Ground-based instrumentation included a CW Doppler radar unit for measuring model velocity and acceleration, an NASA modified SCR-584 radar unit for obtaining the model position in space as a function of time, and a spinsonde receiver operating on the telemeter-antenna radiation pattern as an additional measure of the model rolling velocity. Atmospheric conditions and wind velocities over the firing range were obtained from rawinsondes released immediately after the model flights. Manually operated 16-millimeter and 35-millimeter tracking cameras were used to photograph the model flights.

PREFLIGHT MEASUREMENTS

The lifting surfaces for the swept-wing models were very flexible. In order to obtain stiffness data, one wing and the vertical tail of one model were subjected to concentrated static loads at four points along both the 0.25- and 0.50-chord lines, and the deflections along the leading and trailing edges were measured. The results of the static loading tests are presented as influence coefficients in figure 6. The moments of inertia of all models were determined by swinging the models as pendulums and measuring the frequency of the oscillations. The principal longitudinal

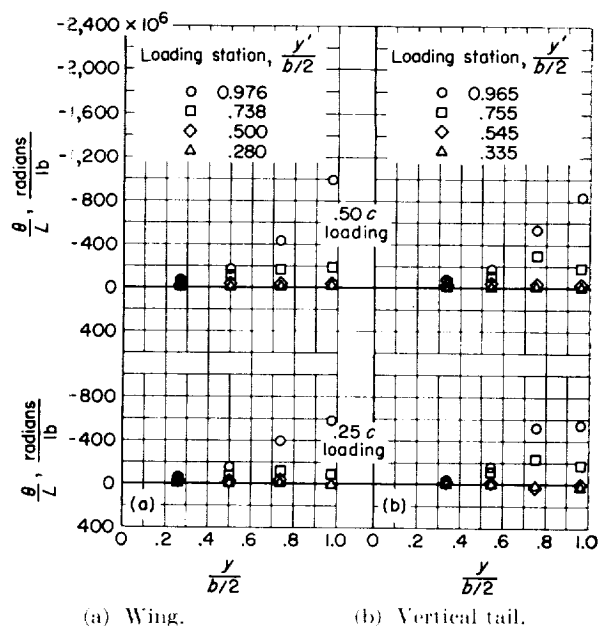
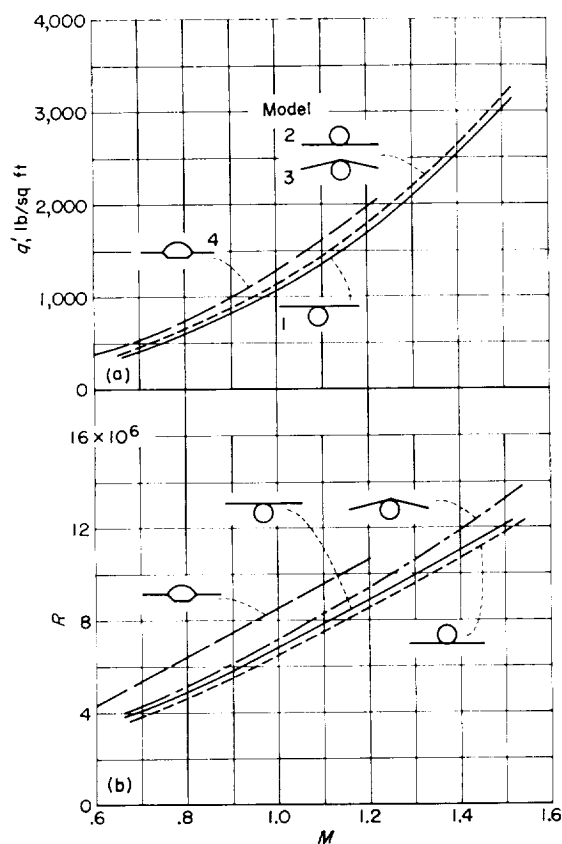


FIGURE 6.—Measured influence coefficients for wing and vertical tail used on swept-wing models.

axis was determined by swinging the models in roll about a number of longitudinal axes inclined at various angles in the plane of symmetry and noting the angle for which the moment of inertia in roll was a minimum.

FLIGHT TESTS

Each model was accelerated to a maximum Mach number between 1.2 and 1.5 by a solid-propellant ABL Deacon rocket motor, which separated from the model after burnout as a result of the relative drag-to-weight ratios. Figure 5 shows model 4 and booster on the launcher. The models contained no sustainer rockets. The yaw disturbers on models 1 to 3 (fig. 3(b)) remained retracted during boosted flight and their operation was started at separation. The yaw vanes were programmed to extend fully in a time of 0.33 second and retract in a time of approximately 0.05 second, the cycle being repeated every 1.4 seconds. Since the yaw vanes were set at a fixed angle of 10° with respect to the model center line, the model assumed a negative sideslip angle with the vanes extended. Upon the rapid retraction of the vanes, the model oscillated about the undisturbed trim conditions. The pulse rockets in model 4 were fired periodically during coasting flight by means of delay squibs. The test conditions prevailing for the flights are presented in figure 7 as a function of Mach number.



(a) Dynamic pressure.
(b) Reynolds number based on mean aerodynamic chord.
FIGURE 7.—Test conditions.

DATA REDUCTION AND CORRECTIONS

Position corrections were required for some of the accelerometer readings to convert the measured values at the instrument location to values at the center of gravity. Corrections for model pitching and yawing velocities were also made to the readings of the air-flow indicators to obtain angles of attack and angles of sideslip. These corrections were made as described in reference 10. In the process of data analysis, all the measured lateral-oscillation data were referenced to β . The frequency-response characteristics of all the instruments were sufficiently close to those of the sideslip vanes so that the only corrections required were to the phase angles of the rolling velocity. These corrections varied between approximately 1° and 5° for the tests herein. The readings from the two transverse accelerometers in each model were used to obtain yawing velocity from the relation

$$\dot{r} = \frac{g(a_{l, nose} - a_{l, cg})}{l} \quad (1)$$

METHOD OF ANALYSIS

TIME-VECTOR SOLUTION FOR OSCILLATORY MOTION

The flight-test oscillation data presented herein were analyzed by the time-vector method for solution of the lateral stability equations of motion (ref. 7). All the measured quantities used in the analysis and the resulting aerodynamic derivatives are referred to the system of body axes illustrated in figure 1. The three equations of motion used to represent the free-oscillation response of the models in the lateral mode following a disturbance are:

$$\frac{mV}{q'S}(\dot{\beta} + r - \alpha p) - C_Y = 0 \quad (2)$$

$$\begin{aligned} \frac{I_X}{q'Sb} \dot{p} - \frac{I_Y - I_Z}{q'Sb} qr - \frac{I_{XZ}}{q'Sb}(\dot{r} + qp) \\ - C_{l\beta}\beta - C_{lp}\frac{pb}{2V} - (C_{lr} - C_{l\dot{\beta}})\frac{rb}{2V} = 0 \end{aligned} \quad (3)$$

$$\begin{aligned} \frac{I_Z}{q'Sb} \dot{r} - \frac{I_X - I_Y}{q'Sb} qp - \frac{I_{XZ}}{q'Sb}(\dot{p} - qr) \\ - C_{n\beta}\beta - C_{np}\frac{pb}{2V} - (C_{nr} - C_{n\dot{\beta}})\frac{rb}{2V} = 0 \end{aligned} \quad (4)$$

In the side-force equation (eq. (2)) the gravity terms $\frac{W}{q'S}(\phi \cos \theta + \psi \sin \theta)$ have been omitted.

As shown in the section entitled "Accuracy," this omission has a negligible effect on the results presented herein and eliminates the necessity of measuring or computing the roll, pitch, and yaw angles. Also in equation (2) the total aerodynamic side force is given by C_Y (which includes the contributions of $C_{Y\beta}$, $C_{Y\dot{\beta}}$, C_{Yp} , and C_{Yr}) because this quantity is obtained from the transverse accelerometer by the relation $C_Y = a_t \frac{W}{q'S}$.

In equations (3) and (4), the assumption has been made that $\dot{\beta} = -r$ in order that the yawing- and sideslipping-velocity derivatives may be combined to reduce the number of unknown aerodynamic terms. As shown by the vector diagrams to be presented later this is a very good approximation for the tests discussed herein. Equations (2) to (4) contain nonlinear inertia terms proportional to α and q . Since α and q are required to be constant in a linear three-degree-of-freedom method of solution, they are assumed constant in the following development.

The fundamental relationships between the various vectors and their derivatives may be

illustrated by considering the solution of equations (2) to (4) for the oscillatory mode of motion resulting from a disturbance. Such a solution may be written in the form

$$\beta = \beta_0 e^{a_1 t} \cos \omega t \quad (5)$$

$$C_Y = \left| \frac{C_Y}{\beta} \right| \beta_0 e^{a_1 t} \cos(\omega t + \Omega_{C_Y}) \quad (6)$$

$$p = \left| \frac{p}{\beta} \right| \beta_0 e^{a_1 t} \cos(\omega t + \Omega_p) \quad (7)$$

$$r = \left| \frac{r}{\beta} \right| \beta_0 e^{a_1 t} \cos(\omega t + \Omega_r) \quad (8)$$

Differentiation of equation (5) gives

$$\dot{\beta} = \sqrt{\omega^2 + a_1^2} \beta_0 e^{a_1 t} \cos\left(\omega t + \tan^{-1} \frac{\omega}{a_1}\right) \quad (9)$$

Also

$$\tan^{-1} \frac{\omega}{a_1} = 90^\circ + \tan^{-1} \frac{a_1}{\omega} \quad (10)$$

and

$$\sqrt{\omega^2 + a_1^2} = \omega_n \quad (11)$$

Thus, the vector representing the derivative of β has a magnitude equal to the magnitude of β multiplied by the undamped natural circular frequency of the motion and a phase angle which leads β by $90^\circ + \tan^{-1} \frac{a_1}{\omega}$ where $\tan^{-1} \frac{a_1}{\omega}$ is referred to as the damping angle. For damped oscillatory motions the damping angle will be positive and for divergent oscillatory motions the damping angle will be negative. Successive differentiations or integrations of any of the components of motion yield the same relationship between vectors and their derivatives. Thus, if any component of motion is measured or otherwise determined in both magnitude and phase angle, the vectors representing any time derivatives of the same component of motion are known as well.

Equations (2) to (4) may then be rewritten in the following form which represents the time-vector method for analysis of the flight data:

$$\frac{mV}{q'S} \left| \frac{\dot{\beta}}{\beta} \right| + \frac{mV}{q'S} \left| \frac{r}{\beta} \right| - \frac{mV}{q'S} \left| \frac{p}{\beta} \right| - \left| \frac{C_Y}{\beta} \right| = 0 \quad (12)$$

$$\begin{aligned} \frac{I_X}{q'Sb} \left| \frac{\dot{p}}{\beta} \right| - \frac{I_Y - I_Z}{q'Sb} \left| \frac{q}{\beta} \right| - \frac{I_{XZ}}{q'Sb} \left| \frac{\dot{r}}{\beta} \right| - \frac{I_{XZ}}{q'Sb} \left| \frac{p}{\beta} \right| \\ - C_{Y_p} \frac{b}{2V} \left| \frac{p}{\beta} \right| - (C_{Y_r} - C_{Y_{\dot{\beta}}}) \frac{b}{2V} \left| \frac{r}{\beta} \right| = 0 \end{aligned} \quad (13)$$

$$\begin{aligned} \frac{I_Z}{q'Sb} \left| \frac{\dot{r}}{\beta} \right| - \frac{I_X - I_Y}{q'Sb} \left| \frac{p}{\beta} \right| - \frac{I_{XZ}}{q'Sb} \left| \frac{\dot{p}}{\beta} \right| + \frac{I_{XZ}}{q'Sb} \left| \frac{q}{\beta} \right| - C_{Y_{\dot{\beta}}} \\ - C_{Y_p} \frac{b}{2V} \left| \frac{p}{\beta} \right| - (C_{Y_r} - C_{Y_{\dot{\beta}}}) \frac{b}{2V} \left| \frac{r}{\beta} \right| = 0 \end{aligned} \quad (14)$$

The amplitude ratios and phase angles required in the solutions are obtained from the time histories of the flight test. Time histories of two typical oscillations for each of the three swept-wing models flown in the experimental program are shown in figures 8, 9, and 10. For convenience in illustrating the important features of the motion, the mean values of rolling velocity have been subtracted from the data and only the disturbances superimposed on these mean values are shown in figures 8 to 10. The essentially steady-state or mean values of rolling velocity were caused by slight amounts of twist in the model wings. From these data the amplitude and phase relations of β , C_Y , and p can be determined for use in the analysis.

Typical vector diagrams are shown in figure 11 for the high-wing model (model 1) and the low-wing model (model 2) for a Mach number of 1.2. The solution is started with the side-force equation. A unit vector β is chosen as shown in figure 11 to establish the scale of the vector diagram.

The vectors $\frac{mV}{q'S} \left| \frac{\dot{\beta}}{\beta} \right|$, $\left| \frac{C_Y}{\beta} \right|$, and $\frac{mV}{q'S} \left| \frac{p}{\beta} \right|$ are then plotted and added vectorially with the proper signs and phase angles by using the values determined from the flight test. The diagram is then closed and the vector representing $\frac{mV}{q'S} \left| \frac{r}{\beta} \right|$ is thus determined. Since $\ddot{\psi}$ or \dot{r} was also measured during the flight tests, the vector $\left| \frac{r}{\beta} \right|$ could have been determined from $\left| \frac{\dot{r}}{\beta} \right|$ as indicated previously.

Instead, the value of $\left| \frac{\dot{r}}{\beta} \right|$ as measured in the flight test is used as a check on the value determined from the vector diagrams.

With a knowledge of $\left| \frac{r}{\beta} \right|$ the solution can then proceed to the rolling-moment and yawing-moment diagrams as shown in figures 11(b) and 11(c). The inertia vectors are first plotted. Data obtained indicate that for the models of the present investigation the lift coefficients, and consequently the pitching velocities, remained near zero. Thus, the rolling- and yawing-moment terms

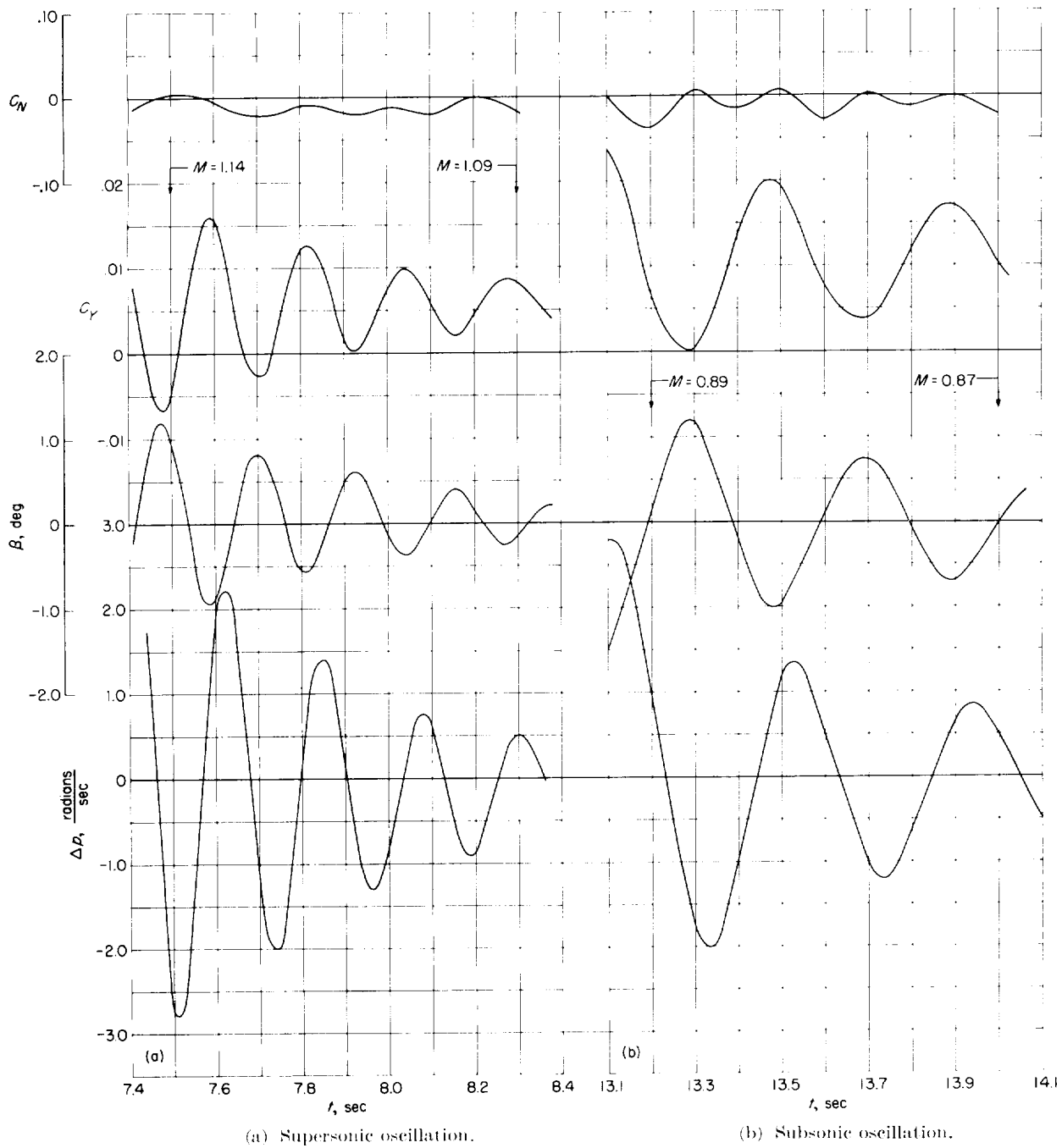


FIGURE 8. Time history of model 1.

proportional to q were negligible and do not appear in the vector diagrams of figure 11. Three vectors representing the aerodynamic derivatives are then required in each diagram but these are known only in direction, not magnitude, and thus not all of them may be determined from the vector solution. Thus, it is necessary either to estimate one of the

rolling-moment and one of the yawing-moment derivatives or to determine them by some other means in order that the other four may be determined. It is logical to estimate those derivatives that are expected to have the smallest effect. In references 9 and 11 and the present investigation, the derivatives generally having the smallest effect

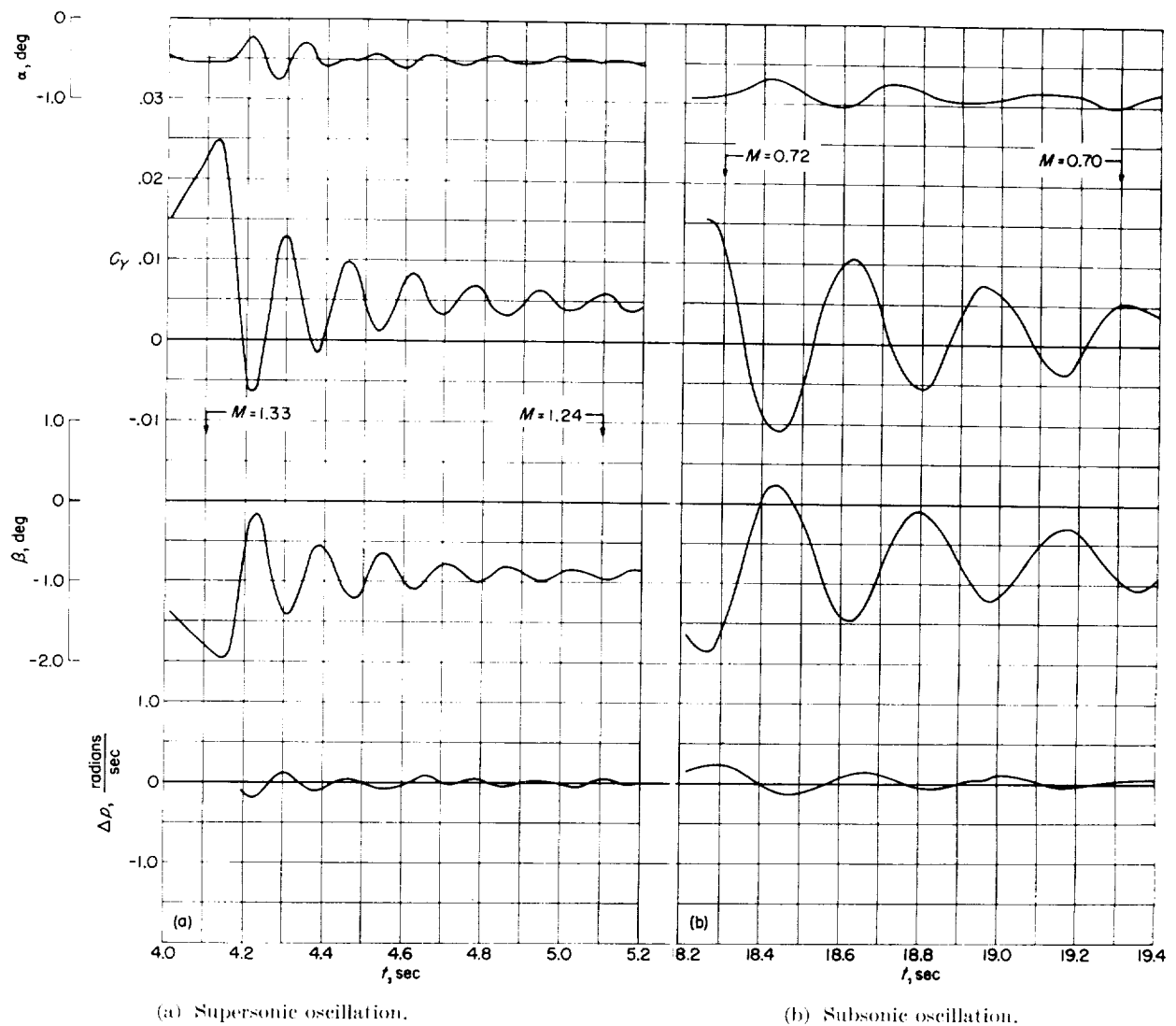


FIGURE 9.—Time history of model 2.

were C_{np} and $(C_{lr} - C_{l\dot{\beta}})$, and estimated values of these derivatives were used for models 1 and 4. For models 2 and 3, however, a somewhat different procedure was used. For the high-wing model (model 1), $C_{lr} - C_{l\dot{\beta}}$ was estimated and then C_{lp} and $C_{l\dot{\beta}}$ were determined from the vector diagrams. It can be seen from figure 11(b) that $C_{lr} - C_{l\dot{\beta}}$ has a relatively minor effect on the motion of the high-wing model. When the same procedure was used for the low-wing model (model 2), very great scatter in the values of C_{lp} occurred and some improbably high and some improbably low values resulted. It is evident in figure 11(b) that $C_{lr} - C_{l\dot{\beta}}$ has a much greater effect on the motion of the low-wing model. Comparisons of the two configurations (both flown at an angle of attack

of nearly 0°) indicated that the contribution of the wing-body combination to C_{lp} should be the same for the two models. Estimations of the contribution of the vertical tails to C_{lp} (ref. 12) showed some differences between results for models 1 and 2 because of the difference in sidewash produced by the rolling wings, but the entire contribution of the vertical tail was less than 5 percent of that due to the wing. Therefore, the values of C_{lp} for the two configurations should be the same within a few percent. On the basis of this reasoning the values of C_{lp} found for model 1 were assumed to apply for model 2, and the vector diagrams were completed to determine $C_{lr} - C_{l\dot{\beta}}$ and $C_{l\dot{\beta}}$.

For model 3 the analysis was similar to that for model 2 except that below a Mach number of

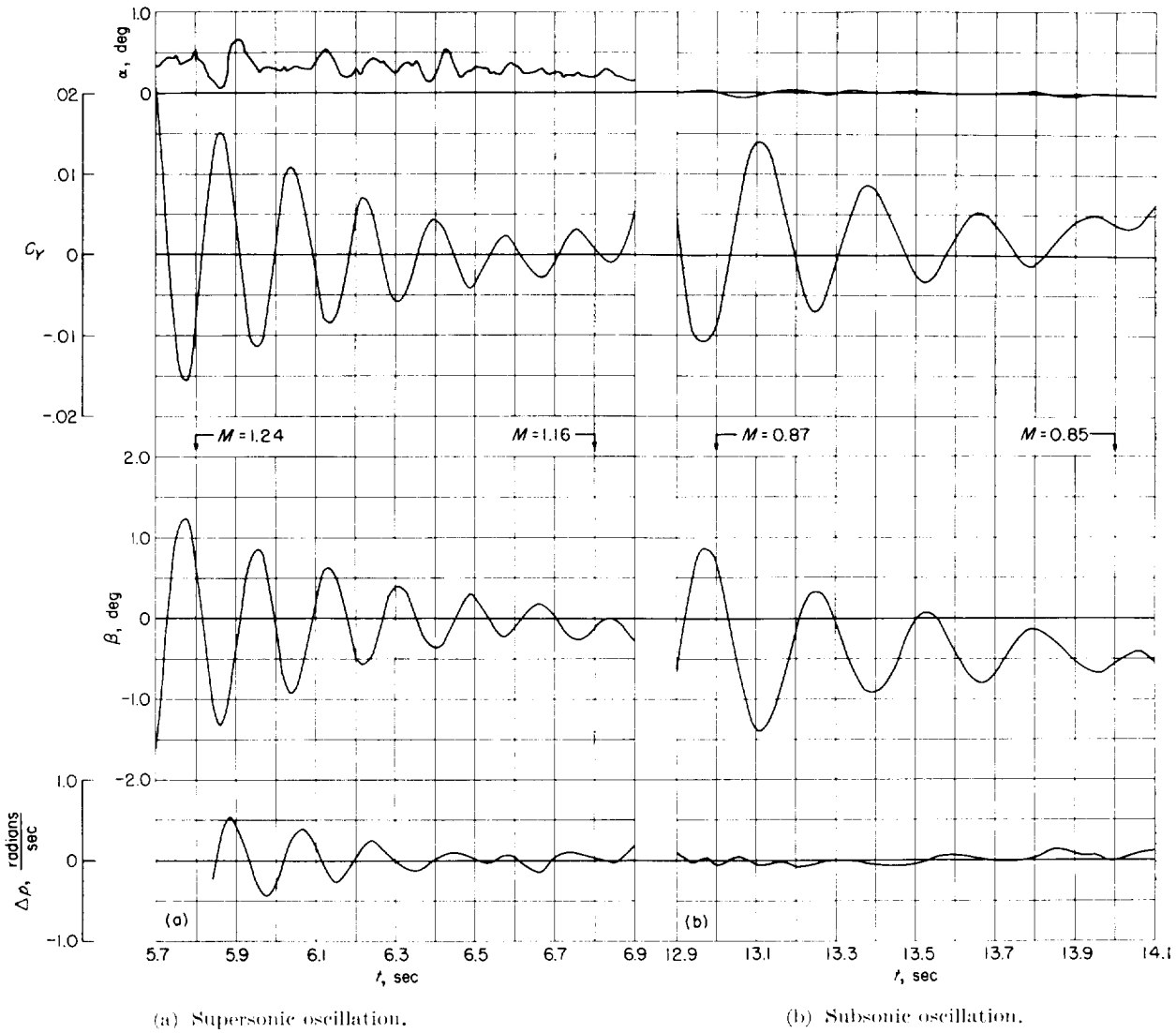


FIGURE 10.—Time history of model 3.

about 0.95 where the rolling motion became essentially zero, all the rolling terms disappeared from the equations and it was not necessary to estimate any of the aerodynamic derivatives.

For solution of the yawing-moment equation, estimated values of $C_{np}=0.02$ for model 1 and $C_{np}=0.05$ for model 2 were used. These values were estimated by use of references 12 to 14 and the difference in value for the two models is due to the difference in sidewash at the vertical tail caused by the rolling wing. The estimated value for model 4 was $C_{np}=0.10$.

QUASI-STATIC METHOD

A quasi-static method outlined in reference 9

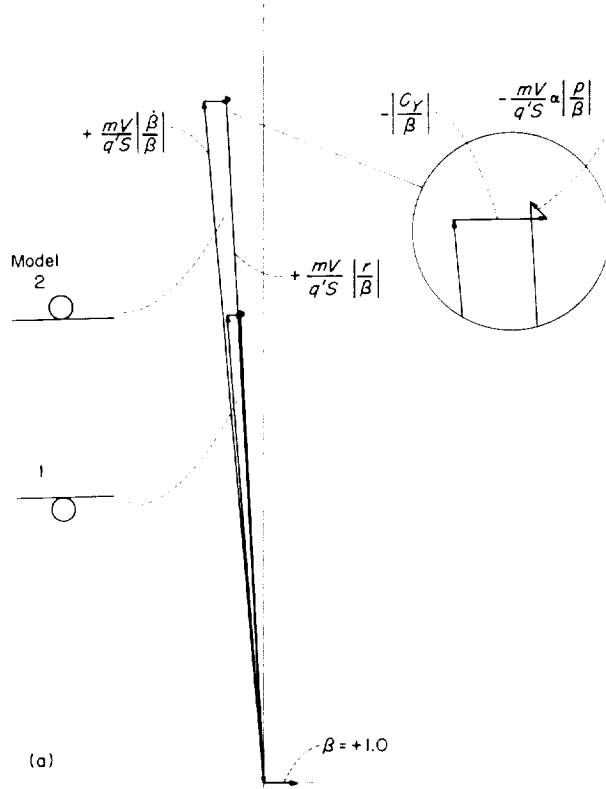
may be used to obtain the lateral-force, yawing-moment, and rolling-moment coefficients. These coefficients can be obtained from equations (2) to (4) as functions of sideslip angle as follows (with the terms involving q assumed to be negligible):

$$C_Y(\beta) = a_t \frac{W}{q'S} \quad (15)$$

$$C_l(\beta) = \frac{I_x}{q'Sb} \dot{p} - \frac{I_{xz}}{q'Sb} \dot{r} - (C_{lr} - C_{l\dot{r}}) \frac{rb}{2V} - C_{lp} \frac{pb}{2V} \quad (16)$$

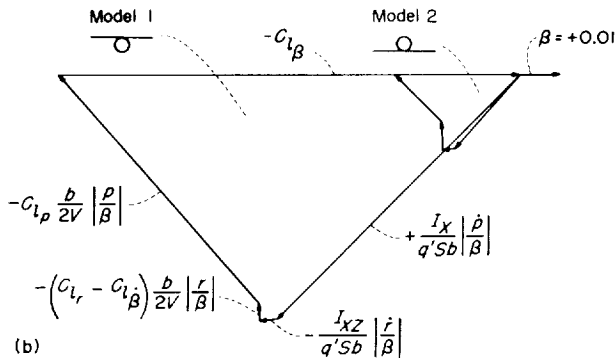
$$C_n(\beta) = \frac{I_z}{q'Sb} \dot{r} - \frac{I_{xz}}{q'Sb} \dot{p} - (C_{nr} - C_{n\dot{r}}) \frac{rb}{2V} - C_{np} \frac{pb}{2V} \quad (17)$$

The side force as a function of sideslip $C_Y(\beta)$ can be taken equal to the total measured side force



(a) Side-force diagram, $\frac{mV}{q'S} \left| \frac{\dot{p}}{\beta} \right| + \frac{mV}{q'S} \left| \frac{r}{\beta} \right| - \frac{mV}{q'S} \alpha \left| \frac{p}{\beta} \right| - \left| \frac{C_Y}{\beta} \right| = 0$.

FIGURE 11. Vector diagrams for high-wing and low-wing models, $M \approx 1.2$.



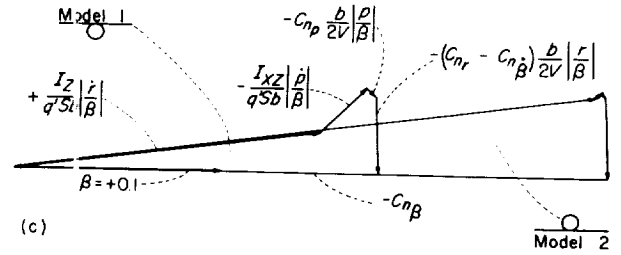
(b) Rolling-moment diagram,

$$\frac{I_X}{q'Sb} \left| \frac{\dot{p}}{\beta} \right| - \frac{I_{XZ}}{q'Sb} \left| \frac{\dot{r}}{\beta} \right| - C_{l_p} - C_{l_r} \frac{b}{2V} \left| \frac{p}{\beta} \right| - (C_{l_r} - C_{l_\beta}) \frac{b}{2V} \left| \frac{r}{\beta} \right| = 0.$$

FIGURE 11.—Continued.

if the measured side force is essentially 180° out of phase with the sideslip angle. This indicates that

$$C_{r_p} \frac{pb}{2V} + C_{r_r} \frac{rb}{2V} + C_{r_\beta} \frac{\dot{\beta}b}{2V} = 0$$



(c) Yawing-moment diagram,

$$\frac{I_Z}{q'Sb} \left| \frac{\dot{r}}{\beta} \right| - \frac{I_{XZ}}{q'Sb} \left| \frac{\dot{p}}{\beta} \right| - C_{n_p} - C_{n_r} \frac{b}{2V} \left| \frac{p}{\beta} \right| - (C_{n_r} - C_{n_\beta}) \frac{b}{2V} \left| \frac{r}{\beta} \right| = 0.$$

FIGURE 11. Concluded.

The rolling and yawing moments as functions of sideslip $C_l(\beta)$ and $C_n(\beta)$, respectively, are given by the total measured moments (\dot{p} and \dot{r} terms in eqs. (16) and (17)) corrected for the moments due to rolling and yawing velocities. The rolling angular acceleration \dot{p} can be obtained from differentiation of the roll rate and the yawing angular acceleration \dot{r} can be obtained from the two transverse accelerometers. The values of the derivatives C_{l_p} and $C_{l_r} - C_{l_\beta}$ are those used in or obtained from the vector solutions, and $C_{n_r} - C_{n_\beta}$, C_{l_p} , and r are obtained from the vector solutions.

A body-axis system was used for the sake of convenience and all flight instrumentation was aligned with the system. The derivatives obtained may be converted to a stability-axis system, but, in this particular case, differences would be small since α is always near zero.

OTHER ANALYSIS PROCEDURES

The time-vector solutions utilize the information available in the oscillatory mode of lateral motion. Other modes of motion exist when a lateral disturbance is applied. These are generally two aperiodic motions; a lightly damped or spiral mode, and a more heavily damped rolling mode. Because of the relatively short testing time available and the changing Mach number for the type of model tests described herein the spiral mode of motion cannot be detected in the flight time histories. The well damped rolling motion can frequently be used to obtain a measure of C_{l_p} , however. An approximation to the damping of this mode of motion can be found by assuming a single degree of freedom in roll with all aerodynamic derivatives zero except C_{l_p} . Solving equation (3) for C_{l_p} under these assumptions

$$C_{l_p} = a_2 \frac{2V}{b} \frac{I_X}{q'Sb} \quad (18)$$

The investigation in reference 15 indicates that generally the factors ignored in obtaining equation (18) will have a negligible effect, except possibly I_{xz} . A somewhat closer approximation may therefore be obtained by including I_{xz} , and solving equations (3) and (4) for this case yields:

$$C_{l_p} = a_2 \frac{2V}{b} \frac{I_x}{q'Sb} - a_2 \frac{2V}{b} \frac{1}{q'Sb} \frac{I_{xz}^2}{I_z} \quad (19)$$

The yaw disturbers and pulse rockets used in the present tests were intended only as disturbers, not as feasible controls. Control surfaces may of course be used to provide disturbances, in which case control effectiveness may also be obtained. An example of such a control surface investigation and control effectiveness analysis is contained in reference 16.

AEROELASTICITY EFFECTS

The flexibility of the wings and vertical-tail surfaces of the swept-wing models described herein had an appreciable effect upon the results. The effects of wing flexibility on C_{l_p} and the increment in C_{l_β} caused by geometric dihedral, and the effects of vertical tail flexibility on C_{Y_β} , C_{n_β} , and C_{n_r} were estimated by the methods given in the appendix.

ACCURACY

The estimated accuracy of the basic measurements is indicated in table III for the high-wing and low-wing models at two Mach numbers. The derivatives C_{Y_β} , C_{n_β} , C_{l_p} , and $C_{n_r} - C_{n_\beta}$ are functions of some or all of the quantities. The incremental error in C_{l_β} , for instance, due to the error in I_x was taken as

$$(\Delta C_{l_\beta})_{I_x} = \frac{\partial C_{l_\beta}}{\partial I_x} \Delta I_x$$

where the partial derivative of C_{l_β} with respect to I_x was obtained from a solution of the vector diagram. The probable error in C_{l_β} due to all the probable errors in table III was taken to be

$$(\Delta C_{l_\beta})_{\text{probable}} = \sqrt{[(\Delta C_{l_\beta})_{I_x}]^2 + [(\Delta C_{l_\beta})_{I_z}]^2 + \dots}$$

Table IV gives the results of this error analysis. The increments due to errors in each of the basic measured quantities are given to illustrate the relative importance of accuracy of each measurement. The results for model 2 should apply approximately to model 3, and the probable

TABLE III.—ESTIMATED ACCURACY OF VARIOUS MEASURED QUANTITIES

[All increments may be positive or negative]

Quantity	Model	Accuracy at —	
		M=1.3	M=0.7
M, percent	1 and 2	1.0	3.0
q', percent	1 and 2	2.0	6.0
t _{1/2} , sec	1 and 2	.03	.10
P, sec	1 and 2	.005	.010
p, sec ⁻¹	1	10	3
β, sec ⁻¹	2	4	2
Ω _p , deg	1	3	3
	2	6	10
W, percent	1 and 2	.5	.5
k _Z ² , percent	1 and 2	1.5	1.5
k _X ² , percent	1 and 2	3.5	3.5
ε, deg	1 and 2	.5	.5
α, deg	1 and 2	.5	.5
β, deg	1 and 2	.5	.5
$\frac{a_1}{\beta}$, percent	1 and 2	2.0	2.0

errors in percent of the derivatives for model 1 apply approximately to model 4. The probable errors in table IV are given in terms of both absolute magnitude and as percentages of the derivatives. The percentage errors have little meaning in some cases, such as for C_{l_β} of model 2 for example, where the absolute error is small but the percentage error is large because C_{l_β} is near zero. Also given are the increments caused by certain amounts of uncertainty in the aerodynamic derivatives that had to be estimated to permit determination of the other derivatives.

From table IV it is evident that the static sideslip derivatives are, in general, more accurately determined than are the rotary derivatives. When the effect of dynamic-pressure inaccuracies (which have an appreciable effect on all derivatives at low speeds) is excluded, the values of C_{n_β} are affected greatly by inaccuracies in P ; the values of $C_{n_r} - C_{n_\beta}$ by inaccuracies in $t_{1/2}$; the values of C_{l_β} by inaccuracies in $\left| \frac{p}{\beta} \right|$; and the values of $C_{l_r} - C_{l_\beta}$ by inaccuracies in Ω_p . When the rolling velocity is large, additional large effects on C_{n_β} and $C_{n_r} - C_{n_\beta}$ are caused by inaccuracies in ϵ and α , and C_{l_p} and C_{l_β} are also affected greatly by inaccuracies in Ω_p . An understanding of the reasons for all these effects can be obtained by a study of the vector diagrams in figure 11.

TABLE IV. CALCULATED ACCURACY OF AERODYNAMIC DERIVATIVES
 [All increments may be positive or negative, and all derivatives are for β in radians]

(a) Model 1

Error in—	$\Delta C_{Y\beta}$ for—		$\Delta C_{n\beta}$ for—		$\Delta C_{i\beta}$ for—		ΔC_{i_p} for—		$\Delta(C_{n_r} - C_{n_b})$ for—	
	$M=1.3$	$M=0.7$	$M=1.3$	$M=0.7$	$M=1.3$	$M=0.7$	$M=1.3$	$M=0.7$	$M=1.3$	$M=0.7$
W	0.003	0.002	0.001	0.001	0.001	0.001	0.001	0.002	0.004	0.004
k_X^2	—	—	.002	.002	.004	.003	—	—	.006	.009
k_X^2	—	—	—	—	—	—	—	.012	—	—
ϵ	—	—	.005	.004	.001	.001	0	0	.140	.113
α	—	—	.003	.005	0	0	0	0	.112	.052
a_L	.011	.009	0	0	0	0	0	0	0	0
β	—	—	.002	.008	.002	.006	.005	.020	.016	.052
q'	.011	.028	0	0	0	.001	.003	.011	.021	.087
$t_{1/2}$	—	—	—	—	—	—	—	—	—	—
P	—	—	.004	.004	.003	.002	.005	.007	.010	.007
p/β	—	—	.001	0	.004	.004	0	.001	.034	.011
M_p	—	—	.004	.004	.005	.005	.022	.035	.032	.032
Omitting weight effects	—	—	0	0	0	0	0	0	.012	.006
Probable error, $\sqrt{\Sigma (\Delta)^2}$.016	.029	.008	.011	.009	.010	.026	.044	.188	.163
Value of derivative	— .561	.470	.119	.126	— .121	.098	— .225	— .330	— .785	— .869
Probable error, percent of derivative*	3	6	7	9	7	10	12	13	24	19
$C_{i_r} - C_{i_b}$ (100 percent error)	—	—	—	—	.002	.003	.013	.022	—	—
C_{n_p} (100 percent error)	—	—	.004	.003	—	—	—	—	.155	.090

*These values apply approximately to model 4.

TABLE IV.—CALCULATED ACCURACY OF AERODYNAMIC DERIVATIVES—Concluded

(b) Model 2*

Error in—	$\Delta C_{Y\beta}$		$\Delta C_{n\beta}$		$\Delta C_{l\beta}$		$\Delta(C_{l_r} - C_{l\beta})$		$\Delta(C_{n_r} - C_{n\beta})$	
	M=1.3	M=0.7	M=1.3	M=0.7	M=1.3	M=0.7	M=1.3	M=0.7	M=1.3	M=0.7
W	0.004	0.004	0.001	0.001	0	0	0	0	0.002	0.003
k_Z^2	---	---	.003	.004	---	---	---	---	.006	.008
k_X^2	---	---	---	---	0	0	.006	.003	---	---
ϵ	---	---	0	0	.001	.002	.004	.004	0	.016
α	---	---	0	0	0	0	0	0	.020	.016
a_t	.018	.014	0	0	0	0	0	0	0	0
β	.018	.043	.004	.014	0	.001	.002	.006	.008	.032
q'	---	---	0	0	0	0	.001	.002	.063	.093
$t_{1/2}$	---	---	.015	.015	.001	.001	.004	.005	.020	.039
P	---	---	0	0	.002	.003	.020	.019	0	0
p/β	---	---	0	0	.001	0	.034	.036	0	.010
Ω_p	---	---	0	0	0	0	0	0	0	0
Omitting weight effect	---	---	---	---	---	---	---	---	---	---
Probable error, $\sqrt{\Sigma(\Delta)^2}$.026	.045	.016	.021	.003	.004	.040	.042	.070	.108
Value of derivative	— .877	— .716	.212	.241	— .017	— .020	.120	.100	— .420	— .540
Probable error, percent of derivative	3	6	8	9	18	20	33	42	17	20
C_{l_p} (0.05 error)	---	---	---	---	.001	.001	.020	.020	---	---
C_{n_p} (100 percent error)	---	---	.001	.001	---	---	---	---	.013	.020

*These results apply approximately to model 3.

The effect of uncertainties in the estimated value of C_{n_p} is fairly large for the yaw damping $C_{n_r} - C_{n_{\dot{\beta}}}$ for model 1 and fairly small for model 2, even though the estimated value is larger for model 2. This effect, of course, is due to the great difference in the amplitude of the rolling motion between the two models. Errors in the values of C_{l_p} and $C_{l_r} - C_{l_{\dot{\beta}}}$ used in the analysis have appreciable effects on each other. However, because of the method of obtaining these derivatives for the present series of tests, as explained in the section entitled "Time-Vector Solutions for Oscillatory Motions," these quantities should be subject to less uncertainty than are the values of C_{n_p} .

RESULTS AND DISCUSSION

Data from the swept-wing models (models 1, 2, and 3) are used to illustrate the use of the time-vector method of solution of the oscillatory motion, and data for the unswept-wing model (model 4) from reference 9 are used to illustrate the usefulness of the quasi-static procedure.

TIME-VECTOR ANALYSIS

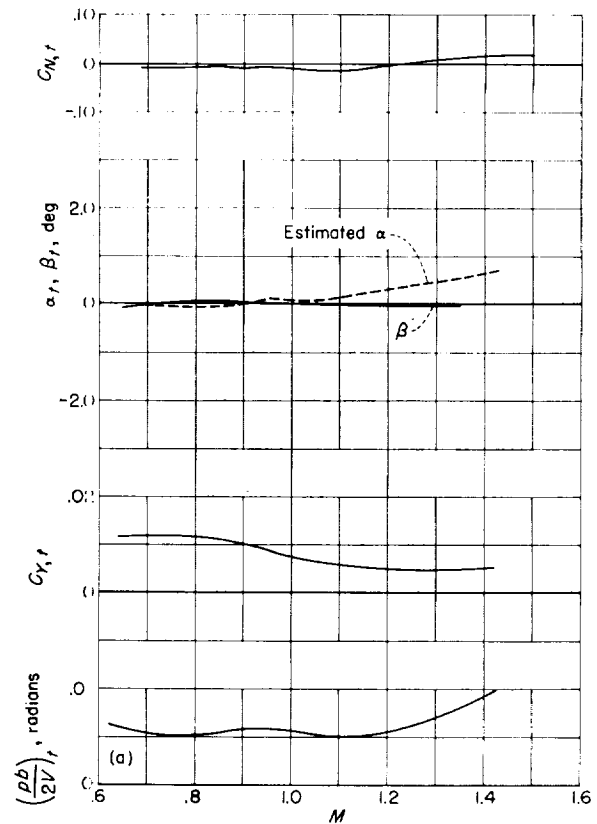
Time histories. Portions of the model time histories for the swept-wing models are presented in figures 8 to 10. The most obvious differences between the motions for the three models are the greatly reduced oscillatory rolling velocities for models 2 and 3 compared with those of model 1. At speeds below about $M=0.9$, model 3 exhibited no discernible periodic rolling motion. Also evident is the lower frequency of the motion for model 1 compared with that of models 2 and 3.

The effects of these motion characteristics on the analysis of the data herein are illustrated in the vector diagrams in figure 11. The larger size of the side-force and yawing-moment diagrams for model 2 than for model 1 is a direct result of the higher frequency for model 2. The larger size of the rolling-moment diagram for model 1 is caused by its higher ratio of rolling to sideslipping motion. The side-force diagram shows that $\dot{\beta}$ and $-r$ are very nearly equal in magnitude and differ in phase angle by only a few degrees; these conditions justify the use of $\dot{\beta} = -r$ in the rolling-moment and yawing-moment equations.

Small variations, mostly of a random character, occurred in the angle-of-attack and normal-force-coefficient time histories; these variations raise the question of inertia coupling between longi-

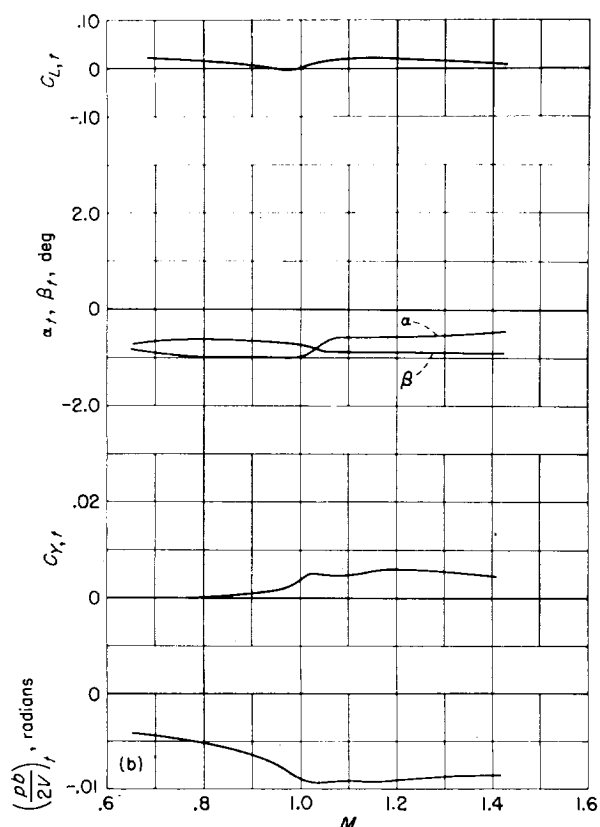
tudinal and lateral motions. Although the effects of the lateral motion on the longitudinal motion were important in producing or modifying the longitudinal motion shown in figures 8 to 10, the factor of significance for the data presented herein is the secondary effect of this longitudinal motion on the lateral motion. Calculations indicated that these latter effects were within the accuracy of the measurements for the data presented herein.

Trim characteristics.—The trim values or mean values of the measured quantities with oscillatory components removed are shown in figure 12. These mean values are a measure of the asymmetry of the models or the measuring instruments. In particular, the positive value of $C_{Y,t}$ for model 1 is believed to represent a constant-acceleration error (or zero shift) in the transverse accelerometer at the center of gravity. This supposition is supported by the mean values not equal to zero which occurred in the values of \hat{r} for this model, as calculated from the difference in readings between the accelerometers at the center of



(a) Model 1. High-wing model.

FIGURE 12. — Model trim characteristics.



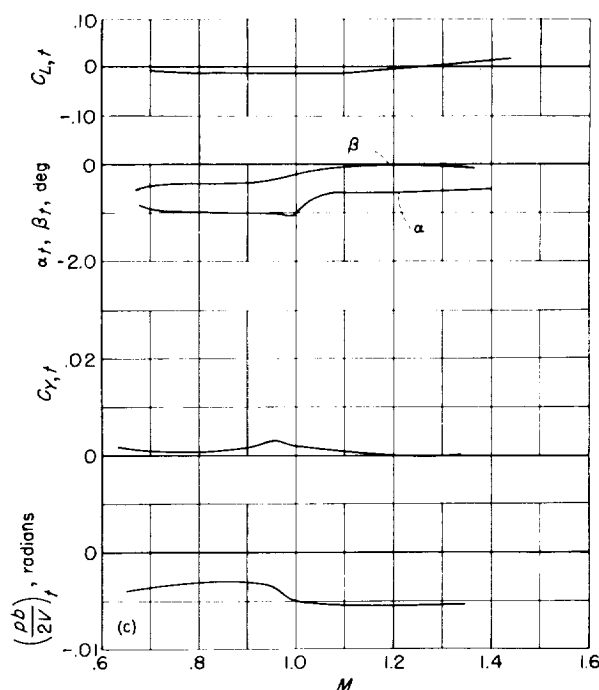
(b) Model 2. Low-wing model.
FIGURE 12. Continued.

gravity and in the nose. Both of these discrepancies are of a magnitude and direction to be explained by the acceleration error.

All models remained near zero lift. The mean values of rolling velocity are given in terms of the helix angle $pb/2V$, which was less than 0.01 for all models. The estimated value of α for model 1 shows the values used in the solution of the equations and was obtained by dividing the measured value of $C_{N,t}$ by an estimated value of $C_{N,\alpha}$, since α was not measured on this model.

Oscillation characteristics.—The measured periods of oscillation are shown in figure 13. The most obvious feature is the larger periods for the high-wing model. The damping characteristics are shown in figure 14. Little difference in magnitude existed between the damping times for the three models.

The amplitude ratios of rolling velocity to sideslip angle are shown in figure 15. The ratio for the high-wing model is 5 to 10 times as high as for the other two models. For both high-wing models, the rolling-velocity amplitude ratio increases con-



(c) Model 3. High-wing model, $\Gamma = -10^\circ$.

FIGURE 12. Concluded.

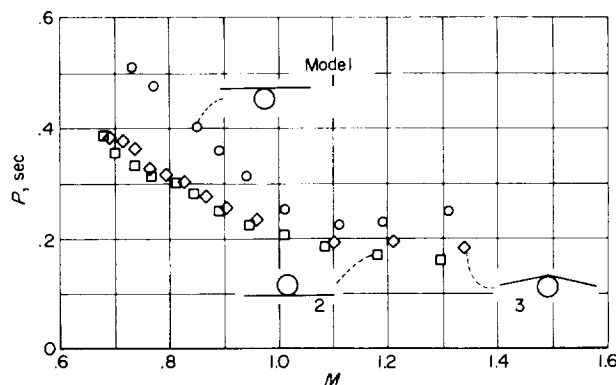


FIGURE 13. Periods of oscillations.

siderably as the Mach number increases, whereas for the low-wing model it is more nearly constant. The -10° dihedral in the high-wing model caused approximately the same decrease in rolling velocity as moving the wing to the low position.

The phase angle by which the rolling velocity leads the sideslip angle is shown in figure 16. Below $M=0.90$, no values could be determined for model 3 because of the lack of any measurable oscillatory rolling velocity. Model 2 exhibits considerably larger variations of phase angle with Mach number than does model 1. At least part of this variation can be attributed to a lesser

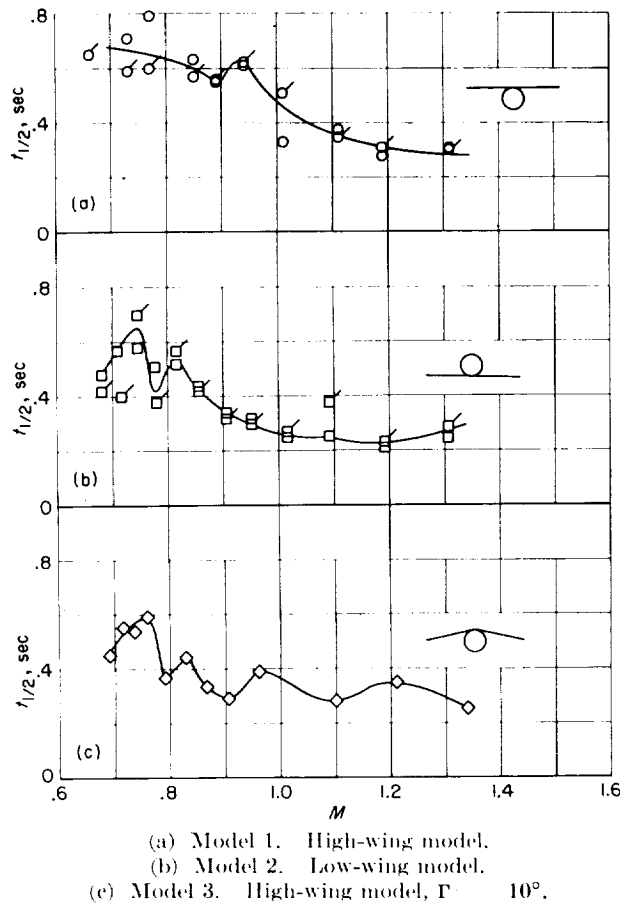


FIGURE 14. Time to damp to one-half amplitude. Unflagged values from β against t . Flagged values from C_Y against t .

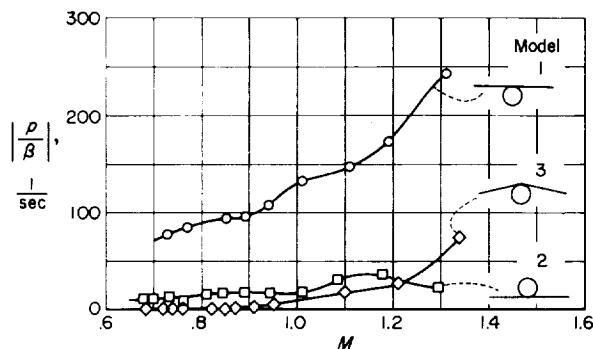


FIGURE 15. Roll-velocity amplitude.

degree of experimental accuracy in determining the phase angles for model 2 because of the smaller amplitudes of rolling motion. This is indicated in table III by the smaller accuracy listed for model 2.

Plots of C_Y against β are shown in figure 17, and the slopes of these curves yielded the derivative $C_{Y\beta}$. Since the phase angle between C_Y

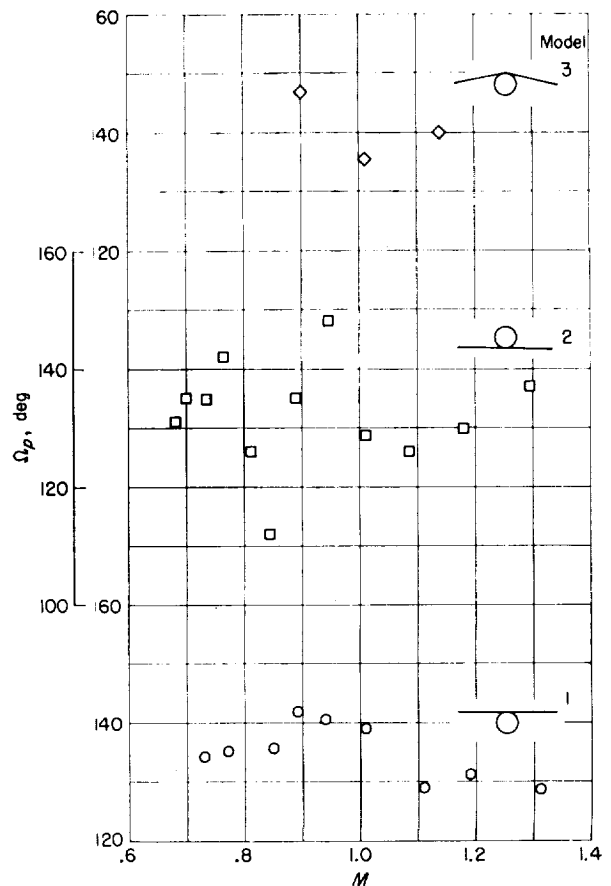
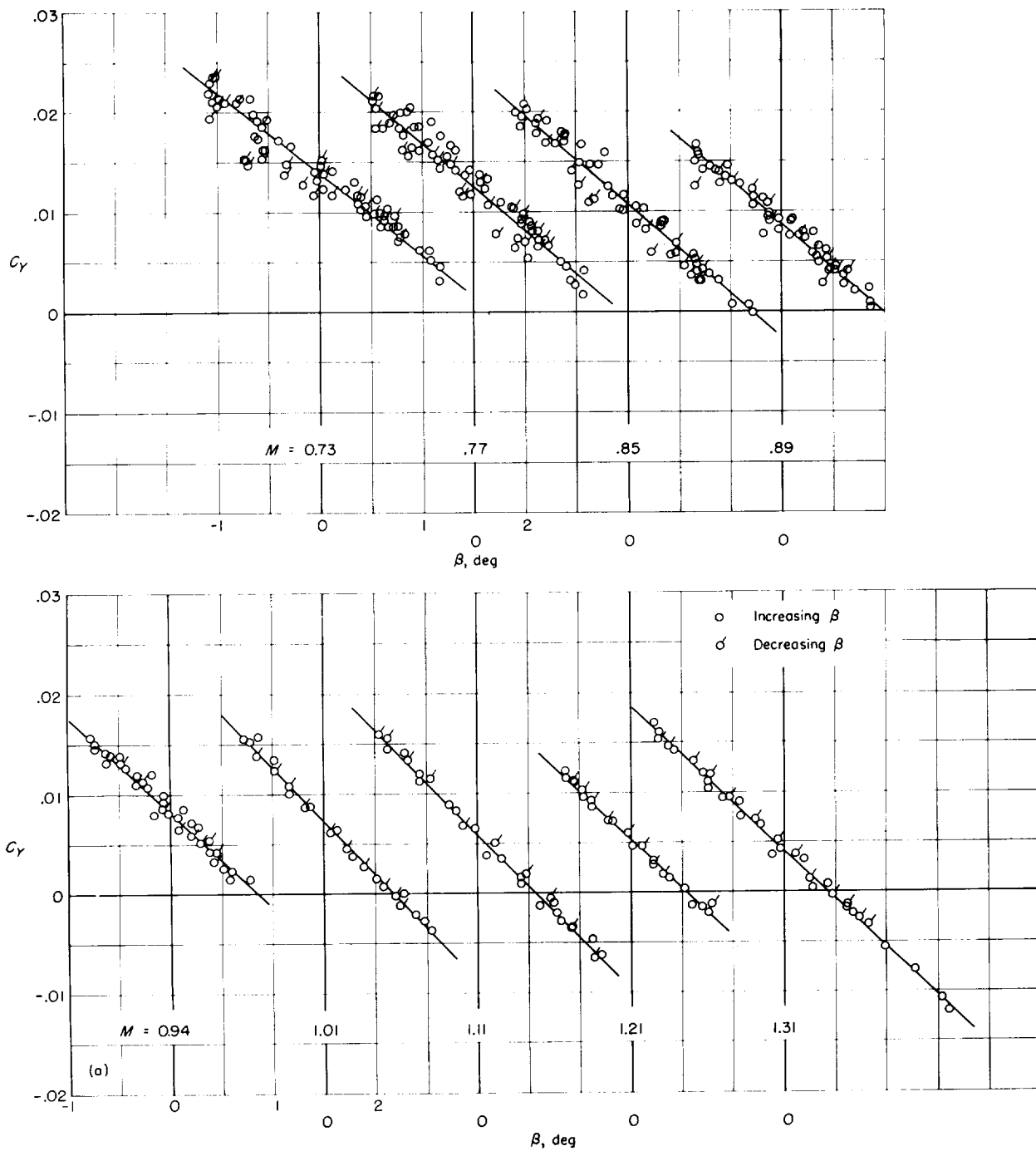


FIGURE 16. Phase angle between rolling velocity and sideslip angle.

and β was 180° for all models within the accuracy to which this quantity could be measured, the amplitude ratio $\left| \frac{C_Y}{\beta} \right|$ required for the vector solution is equal to $-C_{Y\beta}$. Within the random scatter of the data the curves appear to be linear. The slopes faired through the data in figure 17 are those used in the data analysis.

The derivative $C_{Y\beta}$ as a function of Mach number is presented in figure 18. The high-wing model, as would be expected, has lower values of $C_{Y\beta}$ than does either of the other models. In the transonic region the low-wing model has a value of $C_{Y\beta}$ 25 to 50 percent greater than the high-wing model. The values of $C_{Y\beta}$ for the high-wing model with negative dihedral fall between those for the other two models, these values being generally closer to those for the low-wing model. At Mach numbers below 0.9 the slopes $C_{Y\beta}$ for model 3 exhibit some rather large and irregular variations with Mach number for some unknown



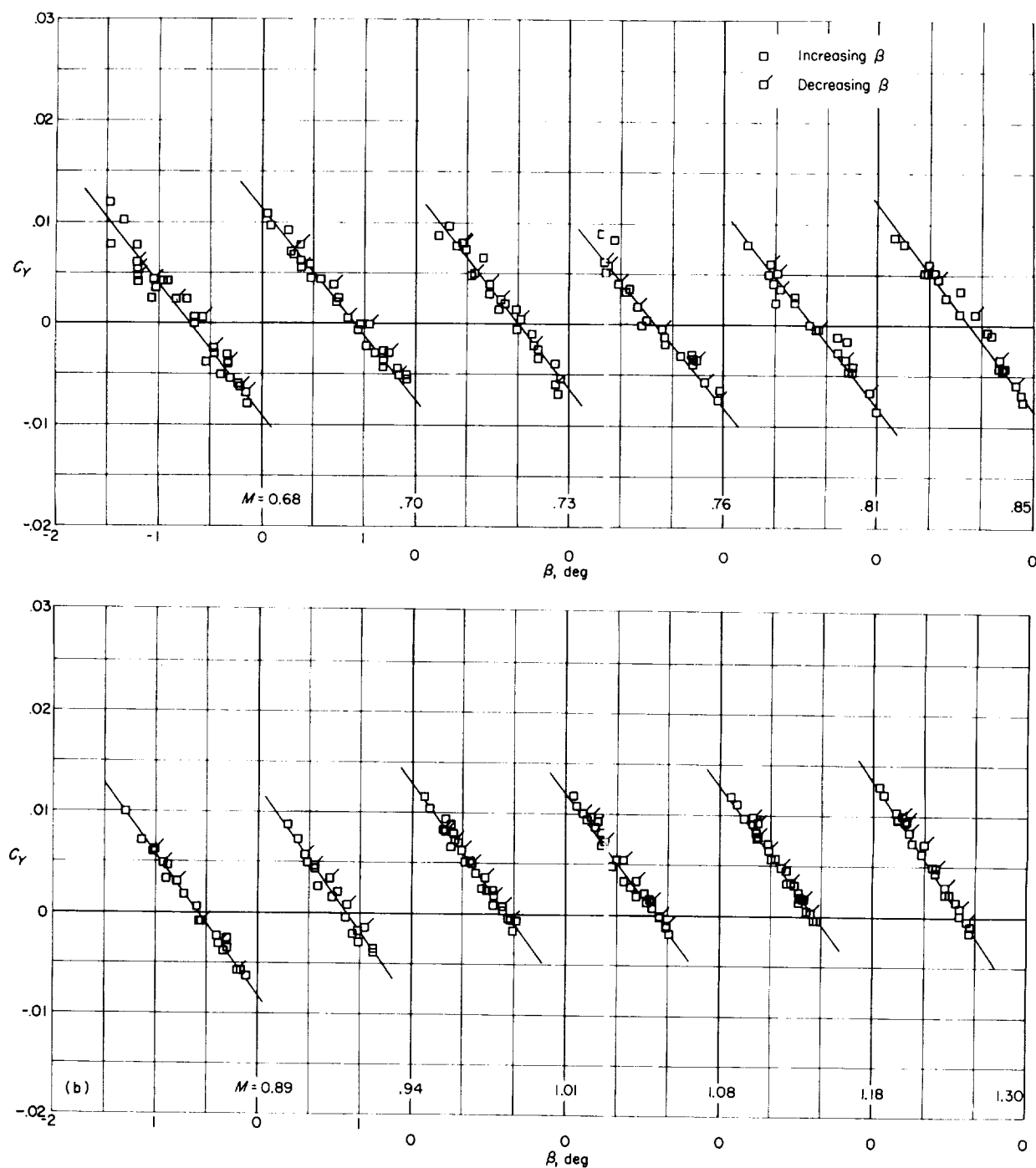
(a) Model 1. High-wing model.

FIGURE 17. Lateral-force coefficients.

reason. Vertical-tail flexibility had a relatively small effect on $C_{Y\beta}$.

The preceding plots (figs. 12 to 18) present the basic information which, with the mass and inertia characteristics given in tables I and II, constitute

the data necessary to construct the vector diagrams. Quantities from the plots of period, amplitude ratio, and phase angle were not faired before using them to construct the vector diagrams since each point in effect constitutes a faired value



(b) Model 2. Low-wing model.

FIGURE 17.—Continued.

to the extent that periods, amplitude ratios, and phase angles are for a number of half-cycles of the oscillations. A faired value was used for $t_{1/2}$ in the data reduction because of the difficulty in obtaining an accurate value of this quantity.

Figure 19 shows a comparison of the amplitude ratio of yawing acceleration to sideslip angle for two models as measured from the transverse accelerometers by the relation given by equation (1), and as determined from the vector-diagram solu-

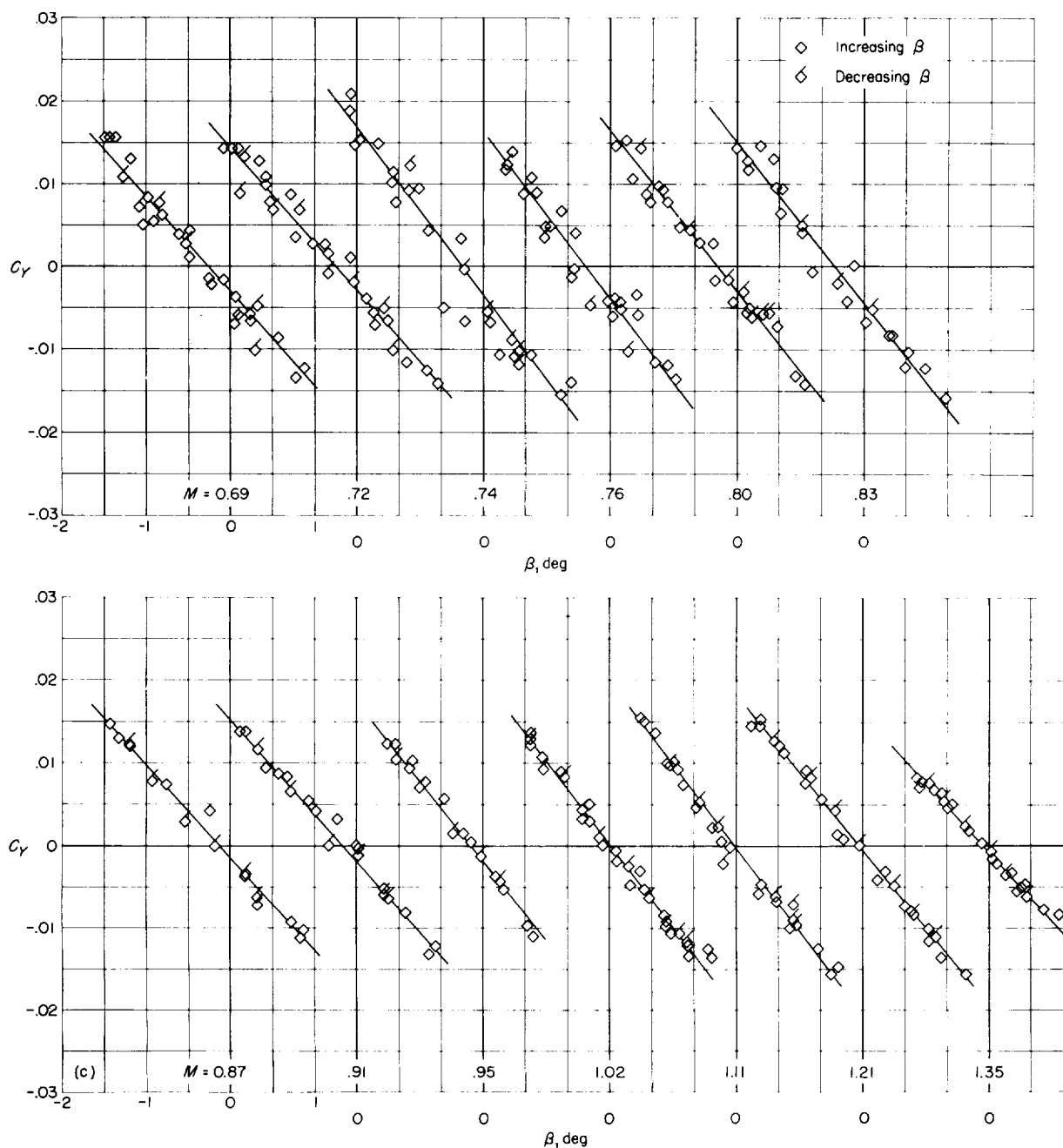
(c) Model 3. High-wing model, $\Gamma = -10^\circ$.

FIGURE 17.— Concluded.

tions. The agreement shown is considered to be very good and furnishes a check on the accuracy of the solutions. The comparison in figure 19 also is a further indication of the small magnitude of coupling effects because the difference in reading between two transverse accelerometers separated along the X -axis will actually be proportional to the sum $(\ddot{x} + pq)$. No phase angle comparison

is shown because an examination of the time histories indicated that the angle Ω_z would have greater inaccuracies than Ω_p (table III) and thus would not furnish any useful information.

Lateral stability derivatives. The sideslip derivatives are presented for β in degrees to facilitate comparisons with wind-tunnel test results. In the equations of motion these derivatives must be

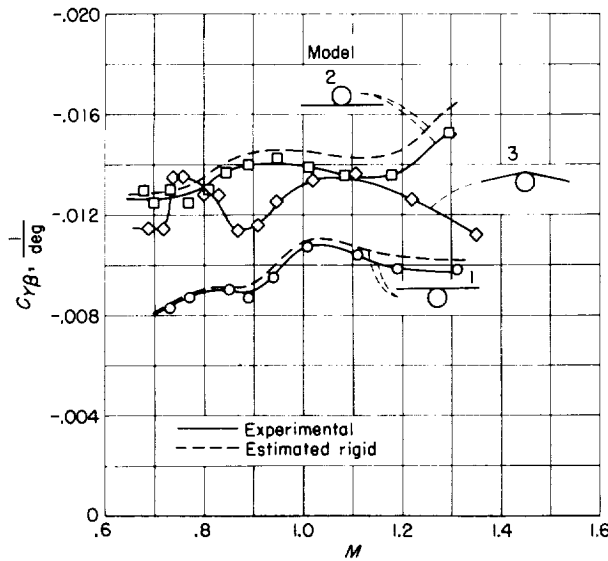


FIGURE 18. Static lateral-force derivative.

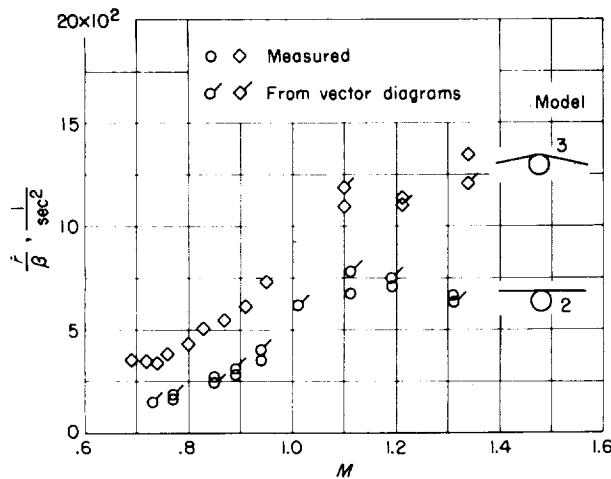


FIGURE 19.—Yawing acceleration amplitude.

used with β in radians. The static stability derivative $C_{n\beta}$ is presented as a function of Mach number in figure 20. In agreement with the high value of sidewash expected for a high-wing configuration (ref. 17), the static stability derivative of the high-wing model is consistently lower than that for either of the other two models. An approximately constant difference exists between the high- and low-wing models. The static stability derivative of model 3 is somewhat lower than that for the low-wing configuration at all Mach numbers. The effect of vertical-tail flexibility is greater for the low-wing model than for the high-wing model because at a given sideslip angle the vertical-tail load is greater for the low-

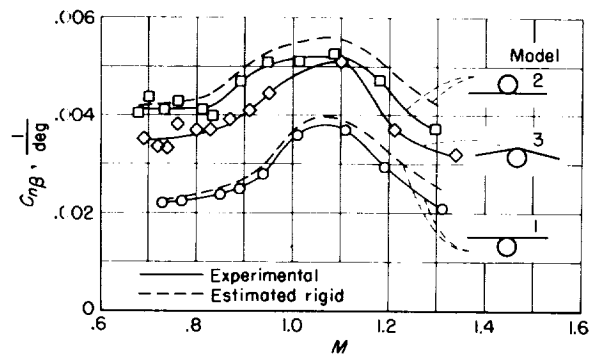


FIGURE 20. Static directional stability derivative.

wing model as a result of the smaller sidewash.

The variation of the effective dihedral derivative $C_{l\beta}$ with Mach number is presented in figure 21. The high-wing model had a large negative value of $C_{l\beta}$ which rose to a peak at $M=1.0$ and decreased in magnitude at supersonic speeds. The values of $C_{l\beta}$ for the low-wing model were approximately one-fourth as large as those for the high-wing model. The variation of the derivative with Mach number for the model with negative dihedral was such that the values of $C_{l\beta}$ were lower than that for the low-wing model at subsonic speeds but increased greatly at Mach numbers above 1.0 and became greater than that for the low-wing model at the highest speeds attained in the tests.

An exact estimate of the effects of flexibility on $C_{l\beta}$ would be very involved since both wing and vertical tail contribute to $C_{l\beta}$, and the wing load distribution and resulting sidewash changes as affected by wing position are unknown. The increment in $C_{l\beta}$ contributed by the vertical tail is

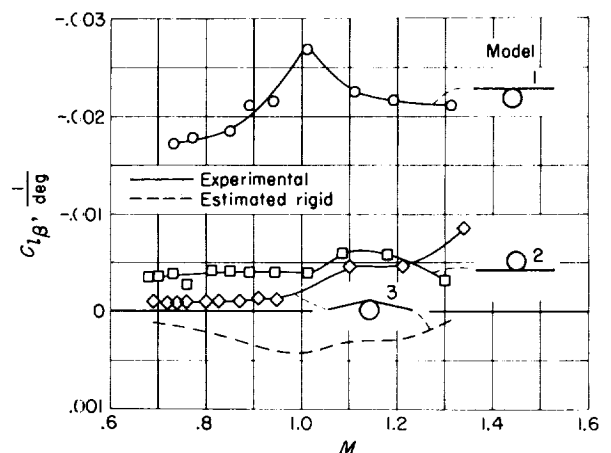


FIGURE 21. Effective dihedral derivative.

reduced by vertical-tail flexibility but this reduction is small (about 9 percent at the highest Mach number) and is nearly the same for all three models. The increment in $C_{l_{\beta}}$ caused by moving the wing to the top or bottom of the fuselage is essentially a wing-root effect and the influence coefficients in figure 6 indicate very little wing twist due to loads concentrated near the inboard end. Therefore, to a first approximation, the values of $C_{l_{\beta}}$ for the high- and low-wing models should be relatively unaffected by wing and tail flexibility. The increment in $C_{l_{\beta}}$ caused by the geometric dihedral is shown by reference 18 and data presented subsequently herein to be approximately proportional to C_{l_p} , although, of course, the load distributions are not identical. Therefore, as a gross approximation, the increments in $C_{l_{\beta}}$ due to geometric dihedral were corrected by the same factor calculated for C_{l_p} and the results are shown in figure 21.

As discussed in the section entitled "Time-Vector Solutions for Oscillatory Motions," the damping-in-roll derivative C_{l_p} was determined for model 1 only and it was assumed that C_{l_p} for models 2 and 3 was the same. Accordingly, the variation of C_{l_p} with Mach number for the three models is shown in figure 22. The effect of wing flexibility on C_{l_p} was very large, the estimated increment due to elasticity being about 50 percent of the measured value at $M=1.3$. The data for C_{l_p} are almost entirely a wing-fuselage effect since, as mentioned previously, the tail surfaces contribute less than 5 percent of the damping in roll when the effect of the rolling wake on the tail is accounted for.

Presented in figure 23 is the variation of the damping-in-yaw derivative $C_{n_r} - C_{n_{\dot{\beta}}}$ with Mach number. As might be accounted for by the high rate of change of sidewash, the damping-in-yaw

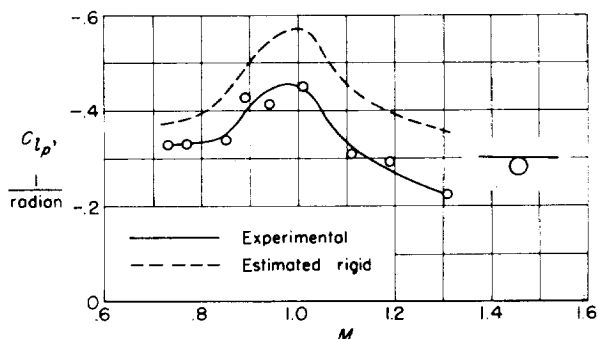


FIGURE 22.—Damping-in-roll derivative.

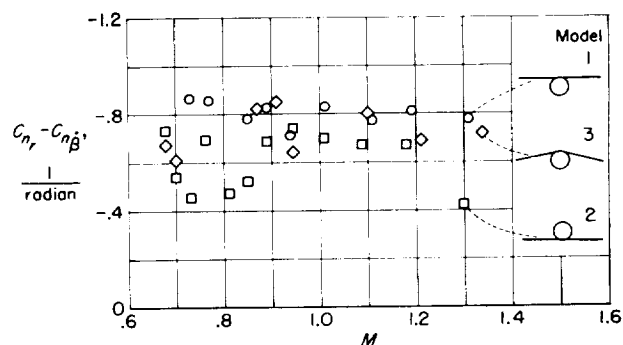


FIGURE 23. Damping-in-yaw derivative.

derivative for the high-wing model is generally higher than the damping for either of the other two models, although the differences approach the order of accuracy (table IV). Both models 2 and 3 show irregular variations in the supersonic region. Flexibility of the vertical tail caused an estimated loss in yaw damping of about 9 percent at the highest Mach number. Since this value is less than the calculated probable accuracy of the derivatives, it is not shown in figure 23.

The variation of the cross derivative $C_{l_r} - C_{l_{\dot{\beta}}}$ with Mach number is shown in figure 24. The solution for the model with negative dihedral at subsonic speed is relatively independent of the assumption for C_{l_p} since the excitation of the roll

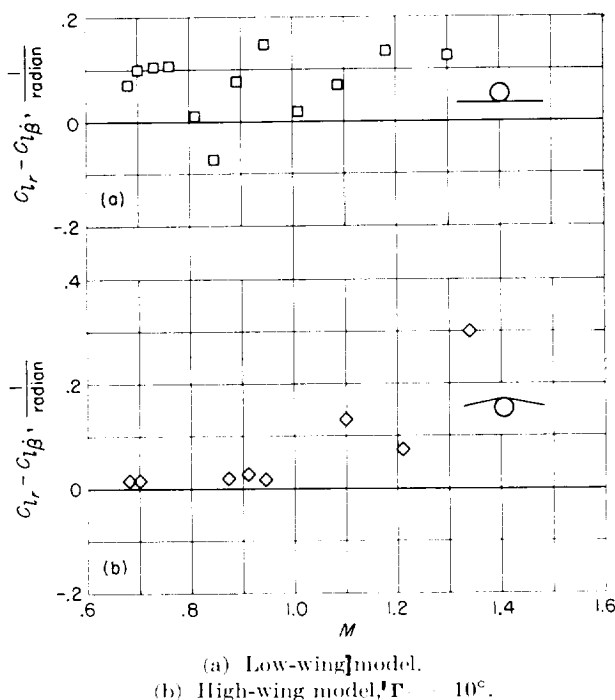


FIGURE 24.—Lateral stability derivative $C_{l_r} - C_{l_{\dot{\beta}}}$.

approached zero below $M=1.0$. Above $M=1.0$, the $C_{l_r} - C_{l_\beta}$ for this model rises rapidly. For the low-wing model, the cross derivative has an erratic variation through the transonic region with a slightly negative value in the region around $M=0.85$. Because of the relatively large possible inaccuracies in this derivative (table IV) and the unknown aerodynamic interference effects, no attempt was made to estimate the effects of flexibility.

Comparison with other data.—Figures 25 and 26 contain summary plots comparing the data described herein with various wind-tunnel, rocket-propelled-model, and theoretical results on similar configurations. The rocket-propelled-model data

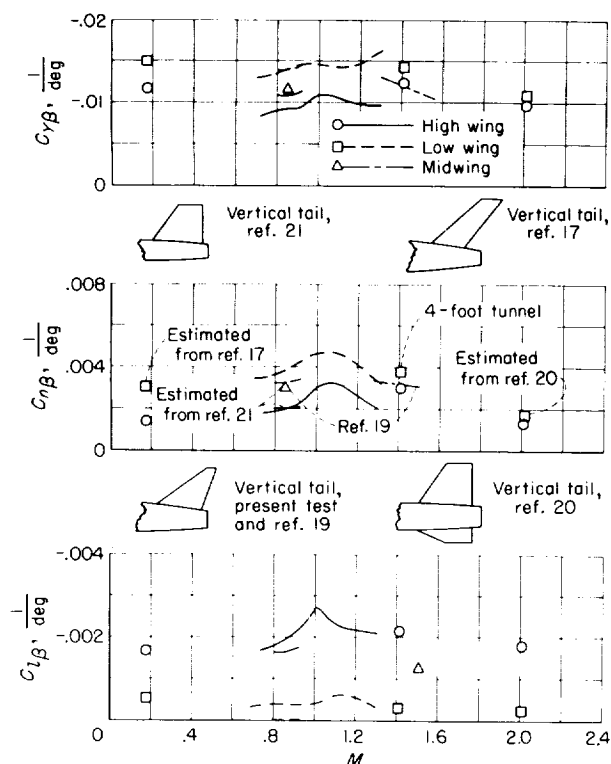


FIGURE 25.—Comparison of rocket-propelled model and wind-tunnel data on effects of wing position.

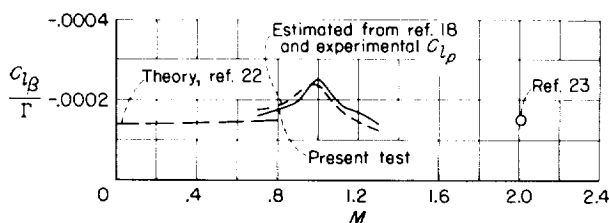


FIGURE 26. Effect of geometric dihedral on the effective dihedral derivative C_{l_β} .

of reference 19 are for wing and tail with the same geometric characteristics as those of the models of the present tests except for a midwing position. The fuselage shape was somewhat different. The wind-tunnel data at Mach numbers of 2.01 (ref. 20) and 1.41 (from tests in the Langley 4- by 4-foot supersonic pressure tunnel) were for the same wing as the present tests but a different empennage arrangement. (See fig. 25.) The wind-tunnel data at $M=0.17$ (ref. 17) and $M=0.80$ to 0.92 (ref. 21) were for configurations with somewhat different wing and tail geometry. All these wind-tunnel data have been corrected for the differences in tail geometry for comparison with the present tests, by estimating the effects of tail geometry but no sidewash changes.

The curves shown in figures 25 and 26 for the present tests are those labeled "estimated rigid" in previous figures since the wind-tunnel data are for essentially rigid models. In addition, the values of C_{n_β} for the present tests have been adjusted to a center-of-gravity position at $0.20\bar{7}$ to furnish a more valid comparison with data in reference 19 (center of gravity at $0.19\bar{7}$) and references 17 and 20 (center of gravity at $0.25\bar{7}$).

Results for the midwing rocket-propelled model of reference 19 agree very well with the sideslip derivatives of the present test (fig. 25) except for C_{n_β} at $M=1.3$ where the values from reference 19 are somewhat higher than would be expected for a midwing configuration from the present tests. The increment in C_{Y_β} and C_{n_β} caused by changes in wing position, at an angle of attack of 0° , are caused by the vertical tail being in different regions of the sidewash field for the different wing positions. These increments for the present test are about the same as those obtained from the subsonic wind-tunnel data of reference 17 where a vertical tail with smaller aspect ratio (lower effective height) was used and are somewhat larger than the increments from reference 21 where a vertical tail with larger aspect ratio (higher effective height) was used. The supersonic wind-tunnel data at $M=1.41$ and $M=2.01$ for a vertical-tail arrangement having part of its area below the fuselage, show much smaller increments resulting from changes in wing height. It could be expected that a vertical tail of small height or one with a portion of its area below the fuselage would result in smaller changes in C_{Y_β} and C_{n_β} due to wing position since the tail would be effectively nearer

the center of the sidewash field and would experience smaller changes in sidewash. A vertical tail having its area symmetrically distributed above and below the longitudinal body axis would produce no change in $C_{Y\beta}$ and $C_{n\beta}$ at an angle of attack of 0° as the wing is moved from the bottom to the top of the fuselage.

The increments in $C_{l\beta}$ caused by changes in wing position (fig. 25) are primarily an effect of the wing and, secondarily, an effect of the tail. These increments are reasonably constant throughout the Mach number range illustrated, some increase occurring at transonic speeds. The comparison between the various sets of data for $C_{l\beta}$ is very good. No theoretical values are shown in figure 25 because no theoretical values of sidewash resulting from the load distributions due to changes in wing position are available.

A summary of the effects of geometric dihedral on $C_{l\beta}$ is shown in figure 26. The approximate method of reference 18 when used with the experimental (flexible) values of $C_{l\beta}$ from the present test showed remarkable agreement with the experimental values. This fact formed the basis for the method of correcting the $C_{l\beta}$ value of model 3 for flexibility as described previously. The subsonic theory of reference 22 and the supersonic wind-tunnel data of reference 23 show values of $\frac{C_{l\beta}}{P}$ similar to those obtained in the present tests.

The values of $C_{l\beta}$ from the present test corrected to rigid-wing values are somewhat higher at subsonic speeds than the theoretical values (ref. 22) and are higher than the theory of reference 24 at $M=1.0$. The curve of $C_{l\beta}$ for the present test (uncorrected for flexibility), when extrapolated, indicates good agreement with the data for $C_{l\beta}$ in reference 20 which were for the same wing and tail arrangement.

Little information exists on the derivative $C_{l_r} - C_{l_{\dot{\beta}}}$ for comparison with the present results. Calculated values from reference 13 at low subsonic speeds were about 0.04 which is at least the correct order of magnitude. (See fig. 24.)

Flying qualities.—The motion characteristics presented previously for the three models may be interpreted in terms of flying qualities for a full-scale airplane. The nondimensional characteristics of the motion—that is, amplitude ratios such as $\left|\frac{\phi}{\beta}\right|$, phase angles, and number of cycles required to

damp to a given fraction of the original amplitude—may be considered as applying directly to a full-scale airplane having the same relative density and the same nondimensional radii of gyration.

The relative density factor μ_b for the model tests varied from about 115 at a Mach number of 0.7 to about 87 at a Mach number of 1.3. The full-scale airplane altitudes and wing loadings represented by these values, the models flown being assumed to be 1/10-scale models, are shown in figure 27. The values simulated by the models are reasonable for current airplanes.

Suggested requirements for damping of the lateral oscillations for airplanes are given in reference 25. These requirements are illustrated in figure 28. Points for all three models discussed herein are shown on the chart for two Mach numbers. It is apparent that the damping is unsatisfactory for all three configurations for normal-flight conditions, according to the proposed boundaries of reference 25.

A comparison was made of the nondimensional radii of gyration of the three models with average values for three current swept-wing fighter airplanes. The comparison showed that the radii of gyration in roll were the same but that the radii of gyration in yaw of the models were about 15 percent larger than those for the full-scale airplanes. Also, as stated previously, the centers of gravity of the models were placed near the leading edge of the mean aerodynamic chords to minimize pitch-yaw coupling. A normal center-of-gravity position for this type of airplane would probably be near 30 percent of the mean aerodynamic chord. The effects on the motion of reducing the radius of gyration in yaw by 15 percent and the effects of this reduction combined with a 30-percent rearward movement of the center of gravity were

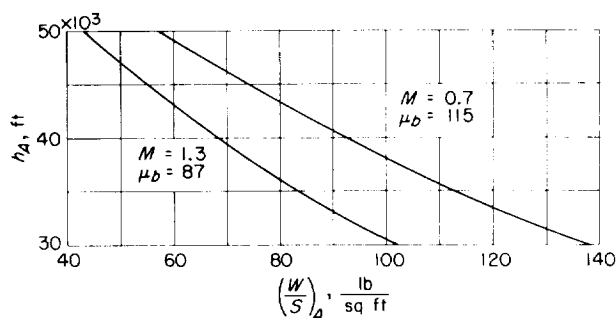


FIGURE 27. Airplane flight conditions simulated by models with 10:1 scale factor and same relative density assumed.

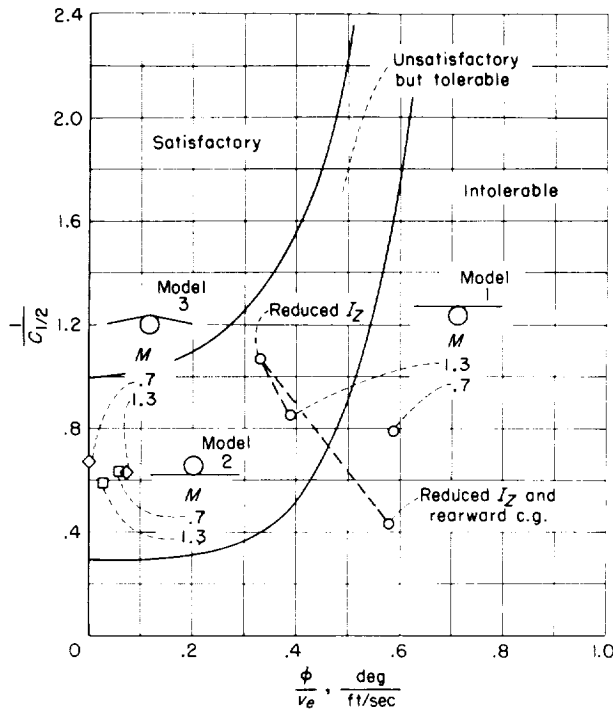


FIGURE 28. Requirements for damping of lateral oscillations.

investigated for the high-wing model at a Mach number of 1.3. This point was chosen since it represents the lowest static stability measured during the present tests and thus would be expected to produce the largest effects. The stability derivative C_{n_β} and the damping derivative $C_{n_r} - C_{n_{\dot{\beta}}}$ were transferred to the altered center-of-gravity position. Since the transfer equations for C_{n_r} and $C_{n_{\dot{\beta}}}$ are different, this procedure cannot be done rigorously since only the quantity $C_{n_r} - C_{n_{\dot{\beta}}}$ is known. Wind-tunnel tests and estimated results, however, indicate that $C_{n_{\dot{\beta}}}$ should be small compared with C_{n_r} at low lift and that C_{n_r} is nearly all caused by the vertical tail. Therefore, the damping derivative $C_{n_r} - C_{n_{\dot{\beta}}}$ was reduced by the square of the ratio of vertical-tail distances from the two center-of-gravity positions. Solutions for these altered conditions were made with the aerodynamic derivatives as known quantities to obtain the motion characteristics. The results are shown in figure 28. Reducing the radius of gyration caused the motion to move closer to the satisfactory region. When this condition was combined with a rearward center-of-gravity movement, the motion became definitely unsatisfactory.

This latter result is contrary to what might be expected if a simple yawing oscillation is considered. The calculations showed that it was caused by the product-of-inertia effect assuming relatively greater importance when the aerodynamic derivatives C_{n_β} and $C_{n_r} - C_{n_{\dot{\beta}}}$ were reduced by the rearward center-of-gravity movement.

An additional desirable quality for the lateral oscillatory motion is that the ratio $\left|\frac{\phi}{\beta}\right|$ should not exceed about 4 (ref. 26) to preclude excessive rolling motions resulting from small corrections in heading or from flight through rough air. Figure 29 shows the values of $\left|\frac{\phi}{\beta}\right|$ for the three models. For the high-wing model, the ratio $\left|\frac{\phi}{\beta}\right|$ remains above 5 for all Mach numbers. For the other two models, $\left|\frac{\phi}{\beta}\right|$ remains below 2 over the Mach number range investigated.

QUASI-STATIC ANALYSIS

The vector method of solution illustrated previously is a linear solution subject to the usual restrictions of such solutions. The aerodynamic derivatives obtained from the vector solution are average or effective values over the amplitude range covered by the solutions. Some insight into the linearity of the static stability

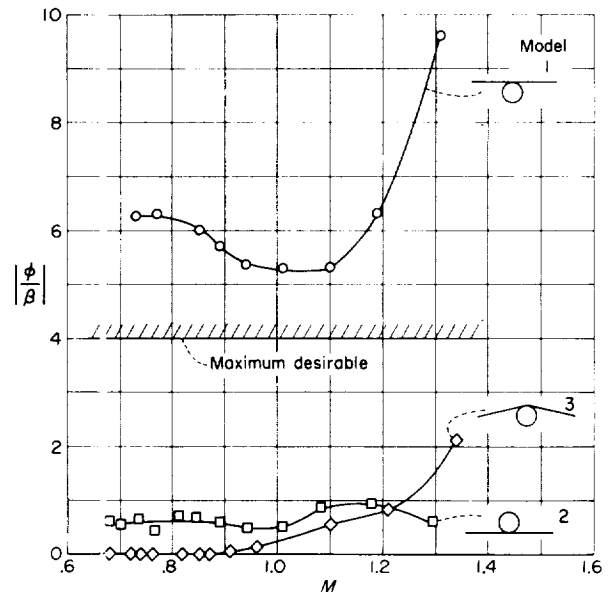


FIGURE 29.—Roll-to-sideslip ratios.

derivatives can be obtained from the quasi-static analysis.

The variation of lateral-force coefficient, yawing-moment coefficient, and rolling-moment coefficient with angle of sideslip and Mach number are shown in figure 30 for the unswept-wing model. These coefficients were obtained as functions of β as indicated in the analysis.

The straight lines through the data points for C_Y , C_n , and C_l are drawn with the slope used in or obtained from vector diagrams. Wind-tunnel data from reference 27 for a Mach number of 0.9 are also shown. The wind-tunnel data indicate a marked reduction in slope at small angles of sideslip, but the slope at moderate sideslip is about the same as that of the present test. The linear variation from the vector solution is in general a good representation of the rocket-propelled-model data; however, a close examination indicates some small nonlinear tendency similar to that of the wind-tunnel results. The fact that the rocket-propelled-model data indicate a more nearly linear variation of force and moment coefficients with angle of sideslip at a Mach number of 0.9 than do the data of reference 27 is most likely due to a Reynolds number effect on the sharp-nose airfoil section. The Reynolds numbers of the wind-tunnel and rocket-propelled-model tests were 2.3×10^6 and 7.4×10^6 , respectively.

EVALUATION OF TEST TECHNIQUE

Time-vector solution.—Analysis of the data for the configurations of the present investigation provided some comparative basis for evaluating the test technique. The most obvious conclusion is that no general statements applicable to all cases can be made and each case must be examined individually to determine the aerodynamic derivatives that can be determined and their resultant accuracy.

One of the difficulties in the test technique is that not all the rolling-moment and yawing-moment derivatives usually included in the equations of motion can be determined. Some approximations may be made to permit the determination of the most important derivatives. One approximation generally made is that $\dot{\beta} = -r$ which reduces the number of unknown derivatives by 2.

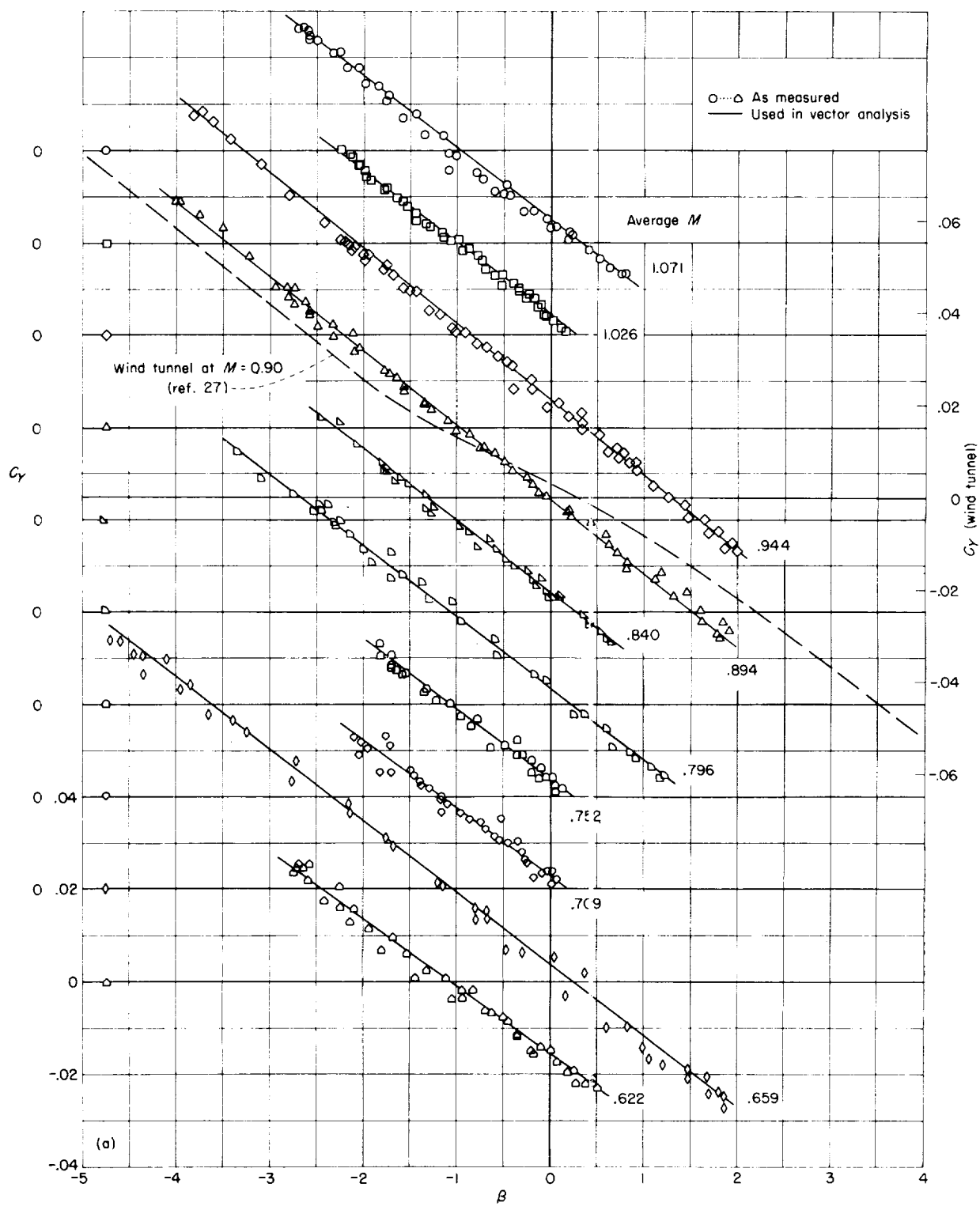
In many cases the cross derivatives C_{Y_p} and

$C_{l_r} - C_{l_{\dot{\beta}}}$ have relatively small effects on the motion and their magnitude may safely be estimated to permit determination of the other derivatives. For some cases where the effects of C_{n_p} or $C_{l_r} - C_{l_{\dot{\beta}}}$ may be appreciable but not necessarily larger than the effects of other derivatives, it may be advantageous to use estimated values of some of the other derivatives such as $C_{l_{\dot{\beta}}}$ or C_{l_p} because of the relatively greater amount of information available from other sources on these derivatives.

It is also fairly obvious that the rolling derivatives C_{l_p} and $C_{l_{\dot{\beta}}}$ are best obtained from motions involving a large ratio of rolling motion to yawing motion and the yawing derivatives $C_{n_{\dot{\beta}}}$ and $C_{n_r} - C_{n_{\dot{\beta}}}$ are best obtained from motions having a large ratio of yawing motions to rolling motion, because these conditions tend to minimize the effects of the cross derivatives. Conversely, the effects of the cross derivatives can be increased by reversing these conditions. Thus, intelligent planning of the dynamic conditions of the tests can result in emphasizing the derivatives of most interest.

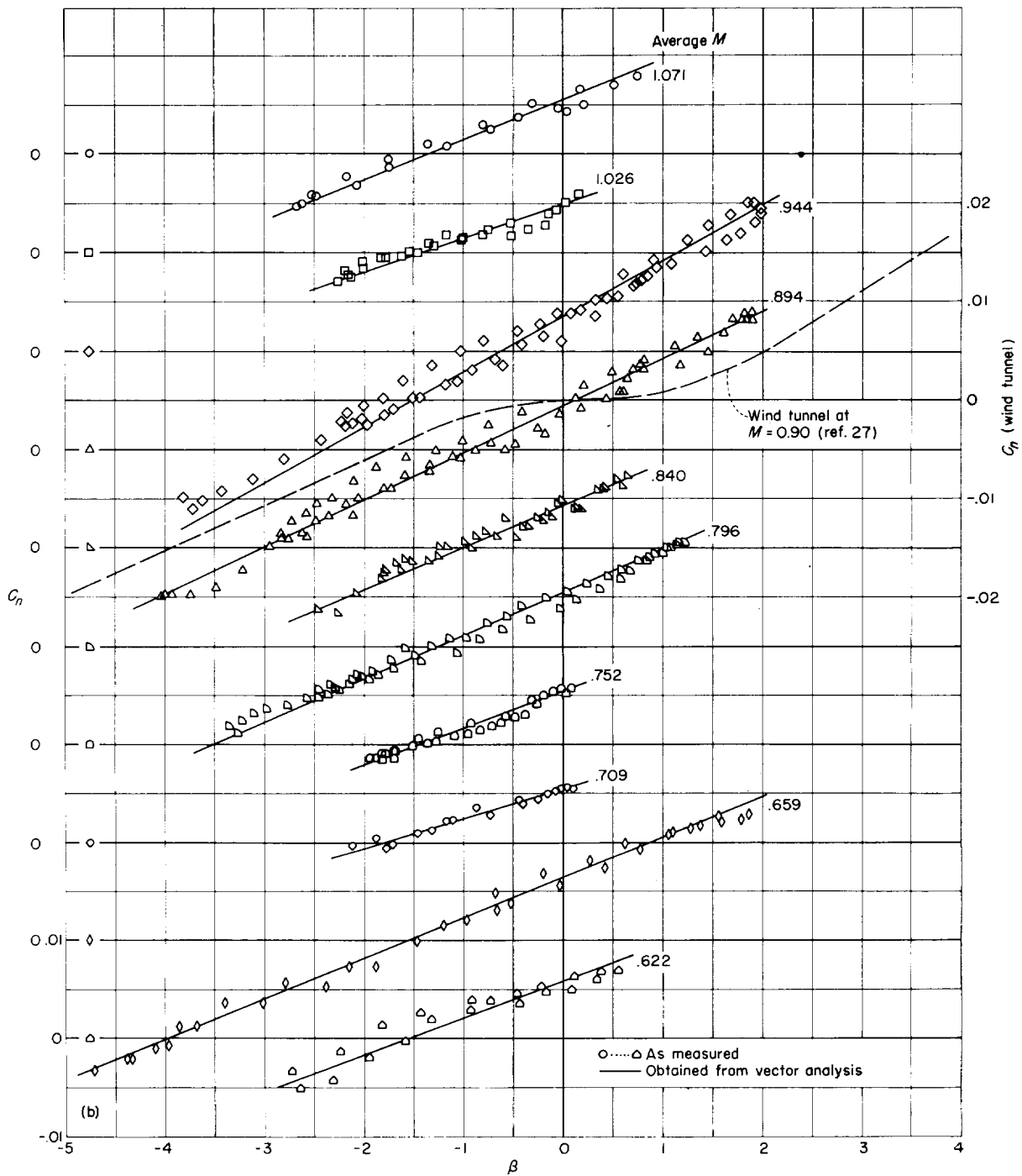
Alterations in the ratio of rolling motion to yawing motion may be accomplished by changing the ratio of rolling moments of inertia to yawing moments of inertia. If two flights at two different inertia ratios but under otherwise identical conditions can be made, then the difficulty of having too many derivatives to measure can be obviated, because two different sets of motions would be available. Both sets of motions must be produced by the same derivatives, and thus a larger number of derivatives may be determined.

As pointed out in the section entitled "Method of Analysis," other modes of motion, such as the heavily damped roll subsidence may be used to assist in analyzing the data. The damping of this motion may be used to find C_{l_p} if this mode of motion can be extracted from the measured time histories. This procedure has been used in other rocket-propelled model tests to measure C_{l_p} . For the present tests the time to damp to half amplitude of this mode of motion was about 0.03 second at $M=1.13$ and 0.06 second at $M=0.7$ and examination of the time histories indicated that this motion could not be extracted from the results. Greater excitation of this mode of motion can be obtained by applying a rolling-moment disturbance rather than a yawing-moment disturbance as for the present tests.

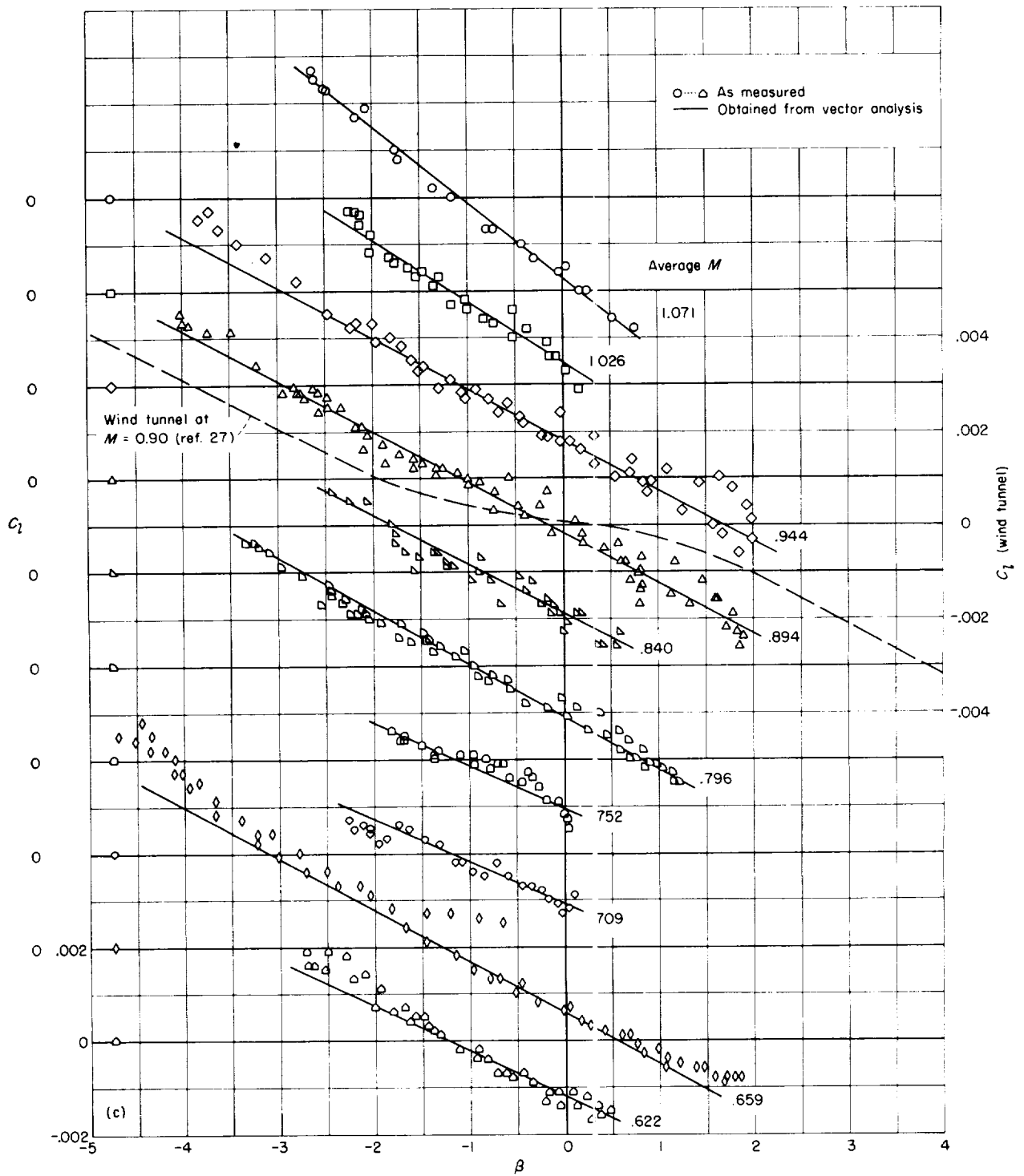


(a) Lateral force.

FIGURE 30. Variation of lateral force, yawing moment, and rolling moment with angle of sideslip and Mach number.



(b) Yawing moment.
FIGURE 30.—Continued



(c) Rolling moment
FIGURE 30.—Concluded.

It would be possible to eliminate the transverse accelerometer, to use a rate gyro to measure r , and to solve the side-force diagram to obtain $C_{Y\beta}$. The diagrams of figure 11(a) indicate that for the dynamic conditions of these tests this procedure would lead to large probable errors in $C_{Y\beta}$ because the phase difference between $\dot{\beta}$ and r , which is principally dependent upon $C_{Y\beta}$, is of the same order of magnitude as the possible phase-angle errors of the rate gyro instruments used (table III). Fairly large errors in $C_{n_r} - C_{n\dot{\beta}}$ would also result from this procedure because these derivatives are greatly dependent on the phase angle between \dot{r} and β (fig. 11(c)).

Although the test technique used is a dynamic technique, the analysis of these and other flight test data indicated that the so-called static sideslip derivatives can usually be determined more accurately than can the rotary derivatives. The rotary derivatives depend primarily on the phase relations between the various components of motion, and a more accurate determination of the rotary derivatives would require greater accuracy in the measurement of the phase angles and of those quantities which effectively cause phase shifts in the motion, such as angle of attack, inclination of the principal axis, and the damping of the motion. The requirement for accuracy of measurement of the phase angles also requires that the frequency-response characteristics of each instrument be known, since appreciable errors in phase angles due to imperfect instrument response may be present in the data and must be corrected for.

For the data presented herein, an angular velocity instrument was used to measure the phase angle Ω_p as well as the rolling velocity, whereas in reference 11 an angular accelerometer instrument was used to measure the phase angle between rolling acceleration and sideslip angle as well as the magnitude of rolling acceleration. The corrections that had to be applied to the measured phase angles due to the frequency responses of these two instruments amounted to about 1° to 2° for the angular velocity instrument and about 16° for the angular accelerometer instrument at $M=1.10$. From a consideration of accuracy, use of an instrument requiring small corrections appears desirable. In fact, it appears worthwhile to determine experimentally the

frequency-response characteristics of the instruments in order to obtain an accurate correction to be applied to the measured phase angles.

In using the present equations of motion and method of solution, the motion being analyzed is assumed to be a linear three-degree-of-freedom lateral motion, with the longitudinal motion parameters (α , q , etc.) remaining constant. Such a condition seldom exists. To permit application of this method, it is important that any unwanted pitching motion remain small. Examination of the data and calculation of the frequency of the longitudinal motion and the magnitudes of the coupling terms for the models of the present investigation indicated that negligible longitudinal-lateral coupling existed. Cases have been encountered in which large pitch-yaw coupling was present (e.g., ref. 28) and it was necessary to include additional terms in the equations of motion and use a least-squares form of solution. For all the models of the present investigation the lift coefficients and, consequently, the pitching velocities remained near zero. Thus, rolling-moment and yawing-moment terms proportional to q were negligible. For tests in which the value of q is appreciable these terms can be included in the time-vector method of solution as long as q remains reasonably constant during each oscillation. It can be seen from the equations and vector diagrams that such terms would have the same effect on the motion as the aerodynamic terms C_{l_r} , C_{l_p} , C_{n_r} , and C_{n_p} .

Quasi-static method.—The quasi-static method furnishes valuable information on the linearity of the static stability data. It also furnishes a check on the accuracy of the vector solution for the static moment derivatives. The use of this method does of course require the assumption of linearity for those quantities which are obtained from the vector solution and then used in equations (16) and (17) to calculate incremental moments or corrections for the purpose of isolating the static stability data; however, this is generally not a serious limitation. The incremental moments so calculated arise from very small air flow angularity changes on the lifting surfaces as caused by rotational velocities and linearly accelerated motion. For example, the largest rolling velocity encountered on the unswept-wing model was about 5 radians per second, which corresponds to

a change in angle of attack at the wing tip of about 0.6° . It would not be expected that those aerodynamic phenomena causing nonlinearities with angle of attack would be felt at such small angles.

In addition, the incremental moments due to the rotational and linearly accelerated motion are usually small compared to the moments due to sideslip. This is particularly true for the yawing-moment equation. It is less true for the rolling-moment equation, in which the moment due to roll damping may be of the same order of magnitude or even larger than that due to sideslip for some cases. Judgment must be used in such cases to assess the value of the method.

CONCLUDING REMARKS

A method of testing and data analysis has been presented for investigating the lateral stability characteristics of airplane models in free flight. The method was illustrated by test results presented for three swept-wing models differing only in vertical position and dihedral of the wing and one unswept-wing model. The time-vector method of solution of the oscillatory motion proved to be a feasible and rapid method of data analysis for determining aerodynamic derivatives. One limi-

tation of the method is that it does not permit determination of all the desired aerodynamic derivatives from one set of flight-test data. Either additional modes of motion or additional test data for other flight conditions may be used to assist in determining some of the aerodynamic derivatives, or those derivatives having a minor effect on the motion may be estimated to permit a solution for the remaining derivatives.

The test and analysis procedure used herein was adequate for establishing the magnitude of the effects of wing position and dihedral for the swept-wing configuration investigated. The measured aerodynamic effects of wing position and dihedral correlated well with available experimental and theoretical data and were of similar magnitude at transonic speeds to wind-tunnel data at subsonic speeds. The quasi-static method of analysis permitted a determination of the effects of Reynolds number on the linearity of the static stability derivatives for an unswept-wing configuration by comparison with wind-tunnel data.

LANGLEY RESEARCH CENTER,
NATIONAL AERONAUTICS AND SPACE ADMINISTRATION,
LANGLEY FIELD, VA., May 4, 1956.

APPENDIX

EFFECTS OF FLEXIBILITY OF VERTICAL TAIL AND WING

VERTICAL TAIL

The effect of vertical-tail flexibility on the vertical-tail lift-curve slope was calculated by the method given in reference 10. For this calculation the influence coefficients in figure 6 and the span-load distributions of reference 29 were used. The loss in vertical-tail lift-curve slope due to flexibility was 9 percent at a Mach number of 1.3 and 1 percent at a Mach number of 0.7. Estimated values for the derivatives $C_{Y_{\beta}}$ and $C_{n_{\beta}}$ for the rigid tail were then obtained from

$$C_{Y_{\beta},r} = (C_{Y_{\beta},e} - C_{Y_{\beta},wf}) \left(\frac{C_{L_{\alpha,rf}}}{C_{L_{\alpha,re}}} + C_{Y_{\beta},wf} \right)$$

and

$$C_{n_{\beta},r} = (C_{n_{\beta},e} - C_{n_{\beta},wf}) \left(\frac{C_{L_{\alpha,rf}}}{C_{L_{\alpha,re}}} + C_{n_{\beta},wf} \right)$$

The values of $C_{Y_{\beta}}$ and $C_{n_{\beta}}$ for the wing-fuselage combination were estimated from wind-tunnel tests.

WING

The effect of wing flexibility on C_{l_p} was calculated by the method of reference 10 with some modifications to obtain rolling-moment effects rather than lift effects. The influence coefficients used are shown in figure 6 and the span-load distribution was obtained from reference 22.

The equations herein represent the right wing of the airplane with a positive load L producing negative rolling moment. The wing and span-load distribution are divided into a number of sections as in reference 10. The equation for C_{l_p} for the elastic wing is

$$C_{l_{p,e}} = \frac{2(m_{X,1} + m_{X,2} + \dots)}{q'Sb \frac{pb}{2V}} \quad (A1)$$

The rolling moment produced by section 1 of the

elastic wing can be approximated by

$$m_{X,1} = C_{l_{p,r}} \left(\frac{pb}{2V} + \frac{\Delta\alpha_1}{\eta_1} \right) q' K_1 \frac{b}{2} \eta_1^2 \quad (A2)$$

where

$$K_1 = S \frac{\int_{\eta_{10}}^{\eta_{1i}} \Gamma(p) \frac{d\eta}{\eta}}{\int_{\eta_0}^{\eta_{10}} \Gamma(p) \eta d\eta}$$

and

$\Gamma(p)$ span-load parameter for rolling wing

$\Delta\alpha_1$ change in section angle of attack caused by wing elasticity

η_1 value of η at centroid of load distribution over section 1

η_0 value of η at root of exposed wing

η_{1i} value of η at inboard end of section 1

η_{1o} value of η at outboard end of section 1

From equation (A2)

$$\frac{\Delta\alpha_1}{pb/2V} = \frac{m_{X,1}\eta_1}{K_1 \frac{b}{2} \eta_1^2 C_{l_{p,r}} q' \frac{pb}{2V}} - \eta_1 \quad (A3)$$

or since

$$m_{X,1} = -L_1 \eta_1 \frac{b}{2} \quad (A4)$$

$$\frac{\Delta\alpha_1}{pb/2V} = \frac{-L_1}{K_1 C_{l_{p,r}} q' \frac{pb}{2V}} - \eta_1 \quad (A5)$$

From the influence coefficients the change in angle of attack at section 1 may be obtained as

$$\frac{\Delta\alpha_1}{pb/2V} = \frac{L_1}{pb/2V} \left(\frac{\theta}{L} \right)_{11} + \frac{L_2}{pb/2V} \left(\frac{\theta}{L} \right)_{12} + \dots \quad (A6)$$

where $\left(\frac{\theta}{L} \right)_{ij}$ is the twist at station i due to a unit

load at station j . Equating (A5) and (A6) and rearranging yields

$$\frac{L_1}{pb/2V} \left[\left(\frac{\theta}{L} \right)_{11} + K_1 C_{l_{p,r}} q' \right] + \frac{L_2}{pb/2V} \left(\frac{\theta}{L} \right)_{12} + \dots = -\eta_1 \quad (\text{A7})$$

Similar equations are written for each section and the resulting set of equations is solved simultaneously for the values of $\frac{L_1}{pb/2V}$, $\frac{L_2}{pb/2V}$, and so forth, for various values of $C_{l_{p,r}} q'$ covering the test range. Then from equations (A1) and (A4) and

the values of $\frac{L_1}{pb/2V}$, $\frac{L_2}{pb/2V}$, and so forth, the ratio of elastic damping in roll to rigid damping in roll is given by

$$\frac{C_{l_{p,e}}}{C_{l_{p,r}}} = - \frac{\left(\frac{L_1}{pb/2V} \eta_1 + \frac{L_2}{pb/2V} \eta_2 + \dots \right)}{C_{l_{p,r}} \zeta} \quad (\text{A8})$$

In addition to its use in correcting C_{l_p} for wing flexibility, equation (A8) was used to give a first approximation to the effects of wing flexibility on the increment of C_{l_β} caused by geometric dihedral, as explained in the section entitled "Lateral stability derivatives."

REFERENCES

1. Ankenbruck, Herman O., and Wolowicz, Chester H.: Lateral Motions Encountered With the Douglas D-558-II All-Rocket Research Airplane During Exploratory Flights to a Mach Number of 2.0. NACA RM H54I27, 1954.
2. Weil, Joseph, Gates, Ordway B., Jr., Banner, Richard D., and Kuhl, Albert E.: Flight Experience of Inertia Coupling in Rolling Maneuvers. NACA RM H55E17b, 1955.
3. Gates, Ordway B., Jr., Weil, Joseph, and Woodling, C. H.: Effect of Automatic Stabilization on the Sideslip and Angle-of-Attack Disturbances in Rolling Maneuvers. NACA RM L55E25b, 1955.
4. Campbell, John P., and Woodling, Carroll H.: Calculated Effects of the Lateral Acceleration Derivatives on the Dynamic Lateral Stability of a Delta-Wing Airplane. NACA RM L54K26, 1955.
5. Campbell, John P., and McKinney, Marion O., Jr.: A Study of the Problem of Designing Airplanes With Satisfactory Inherent Damping of the Dutch Roll Oscillation. NACA Rep. 1199, 1954. (Supersedes NACA TN 3035.)
6. Beam, Benjamin H.: A Wind-Tunnel Test Technique for Measuring the Dynamic Rotary Stability Derivatives at Subsonic and Supersonic Speeds. NACA Rep. 1258, 1956. (Supersedes NACA TN 3347.)
7. Larrabee, E. E.: Application of the Time Vector Method to the Analysis of Flight Test Lateral Oscillation Data. FRM No. 189, Cornell Aero. Lab., Inc., Sept. 9, 1953.
8. Parks, James H.: Experimental Evidence of Sustained Coupled Longitudinal and Lateral Oscillations From a Rocket-Propelled Model of a 35° Swept Wing Airplane Configuration. NACA RM L54D15, 1954.
9. Mitchell, Jesse L., and Peck, Robert F.: Investigation of the Lateral Stability Characteristics of the Douglas X-3 Configuration at Mach Numbers From 0.6 to 1.1 by Means of a Rocket-Propelled Model. NACA RM L54L20, 1955.
10. Gillis, Clarence L., and Mitchell, Jesse L.: Determination of Longitudinal Stability and Control Characteristics From Free-Flight Model Tests With Results at Transonic Speeds for Three Airplane Configurations. NACA Rep. 1337, 1957.
11. D'Aiutolo, Charles T., and Henning, Allen B.: Lateral Stability Characteristics at Low Lift Between Mach Numbers of 0.85 and 1.15 of a Rocket-Propelled Model of a Supersonic Airplane Configuration Having a Tapered Wing With Circular-Arc Sections and 40° Sweepback. NACA RM L55A31, 1955.
12. Michel, William H., Jr.: Analysis of the Effects of Wing Interference on the Tail Contributions to the Rolling Derivatives. NACA Rep. 1086, 1952. (Supersedes NACA TN 2332.)
13. Campbell, John P., and McKinney, Marion O.: Summary of Methods for Calculating Dynamic Lateral Stability and Response and for Estimating Lateral Stability Derivatives. NACA Rep. 1098, 1952. (Supersedes NACA TN 2409.)
14. Margolis, Kenneth: Theoretical Calculations of the Lateral Force and Yawing Moment Due to Rolling at Supersonic Speeds for Sweepback Tapered Wings With Streamwise Tips Subsonic Leading Edges. NACA TN 2122, 1950.
15. Gates, Ordway B., Jr., and Woodling, C. H.: A Method for Estimating Variations in the Roots of the Lateral-Stability Quartic Due to Changes in Mass and Aerodynamic Parameters of an Airplane. NACA TN 3134, 1954.
16. Mitchell, Jesse L., and Vitale, A. James: Free-Flight Investigation of the Control Effectiveness of a Differentially Deflected Horizontal Tail at Mach Numbers From 0.8 to 1.6. NACA RM L56B20, 1956.
17. Goodnan, Alex: Effects of Wing Position and Horizontal-Tail Position on the Static Stability Characteristics of Models With Unswept and 45° Swept-back Surfaces With Some Reference to Mutual Interference. NACA TN 2504, 1951.

18. Purser, Paul E.: An Approximation to the Effect of Geometric Dihedral on the Rolling Moment Due to Sideslip for Wings at Transonic and Supersonic Speeds. NACA RM L52B01, 1952.
19. D'Aiutolo, Charles T., and Henning, Allen B.: Lateral Stability Characteristics Between Mach Numbers of 0.80 and 1.57 and Simulation of Coupled Motion at Mach Number 1.30 of a Rocket-Propelled Model of an Airplane Configuration Having Thin Highly Tapered 45° Sweptback Surfaces. NACA RM L56A17, 1956.
20. Spearman, M. Leroy, Driver, Cornelius, and Hughes, William C.: Investigation of Aerodynamic Characteristics in Pitch and Sideslip of a 45° Sweptback-Wing Airplane Model With Various Vertical Locations of Wing and Horizontal Tail --Basic-Data Presentation, $M=2.01$. NACA RM L54L06, 1955.
21. King, Thomas J., Jr.: Wind-Tunnel Investigation at High Subsonic Speeds of Some Effects of Fuselage Cross-Section Shape and Wing Height on the Static Longitudinal and Lateral Stability Characteristics of a Model Having a 45° Swept Wing. NACA RM L55J25, 1956.
22. DeYoung, John: Theoretical Antisymmetric Span Loading for Wings of Arbitrary Plan Form at Subsonic Speeds. NACA Rep. 1056, 1951. (Supercedes NACA TN 2140.)
23. Spearman, M. Leroy: Investigation of the Aerodynamic Characteristics in Pitch and Sideslip of a 45° Sweptback-Wing Airplane Model With Various Vertical Locations of the Wing and Horizontal Tail --Effect of Wing Location and Geometric Dihedral for the Wing-Body Combination, $M=2.01$. NACA RM L55B18, 1955.
24. Mangler, K. W.: Calculation of the Pressure Distribution Over a Wing at Sonic Speeds. R. & M. No. 2888, British A.R.C., 1955.
25. Liddell, Charles J., Jr., Creer, Brent Y., and Van Dyke, Rudolph D., Jr.: A Flight Study of Requirements for Satisfactory Lateral Oscillatory Characteristics of Fighter Aircraft. NACA RM A51E16, 1951.
26. Williams, Walter C., and Phillips, William H.: Some Recent Research on the Handling Qualities of Airplanes. NACA RM H55L29a, 1956.
27. Olson, Robert N., and Chubb, Robert S.: Wind-Tunnel Tests of a $1/12$ -Scale Model of the X-3 Airplane at Subsonic and Supersonic Speeds. NACA RM A51F12, 1951.
28. Gillespie, Warren, Jr.: Supersonic Aerodynamic Characteristics of a Low-Drag Aircraft Configuration Having an Arrow Wing of Aspect Ratio 1.86 and a Body of Fineness Ratio 20. NACA RM L57A25, 1957.
29. Queijo, M. J., and Riley, Donald R.: Calculated Subsonic Span Loads and Resulting Stability Derivatives of Unswept and 45° Sweptback Tail Surfaces in Sideslip and in Steady Roll. NACA TN 3245, 1954.

